

# Abstract

**Price, Jennifer Lou.** Unsteady Measurements and Computations on an Oscillating Airfoil with Gurney Flaps. (Under the direction of Dr. Ndaona Chokani)

The effect of a Gurney flap on an unsteady airfoil flow is experimentally and computationally examined. In the experiment, the details of the unsteady boundary layer events on the forward portion of the airfoil are measured. In the computation, the features of the global unsteady flow are documented and correlated with the experimental observations.

The experiments were conducted in the North Carolina State University subsonic wind tunnel on an oscillating airfoil at pitch rates of  $65.45^\circ/sec$  and  $130.9^\circ/sec$ . The airfoil has a *NACA0012* cross-section and is equipped with a 1.5% or 2.5% chord Gurney flap. The airfoil is tested at Reynolds numbers of  $96 \times 10^3$ ,  $169 \times 10^3$  and  $192 \times 10^3$  for attached and light dynamic stall conditions. An array of surface-mounted hot-film sensors on the forward 25% chord of the airfoil is used to measure the unsteady laminar boundary layer separation, transition-to-turbulence, and turbulent reattachment. In parallel with the experiments incompressible Navier-Stokes computations are conducted for the light dynamic stall conditions on the airfoil with a 2.5%c Gurney flap at a Reynolds number of 169,000.

The experimental measurements show that the effect of the Gurney flap is to move the separation, transition and reattachment forward on the airfoil. This effect is more marked during the airfoil's pitch-down than during pitch-up. The computational results verify these observations, and also show that the shedding of the dynamic stall

vortex is delayed. Thus the adverse effects of dynamic stall are mitigated by the Gurney flap.

**Unsteady Measurements and Computations on an Oscillating  
Airfoil with Gurney Flaps**

By

**Jennifer Lou Price**

A thesis submitted to the Graduate Faculty of  
North Carolina State University  
in partial fulfillment of  
requirements for the Degree of  
Masters of Science

**Aerospace Engineering**

Raleigh, NC  
July 2001

**Approved by:**



---

**Dr. Ndaona Chokani**  
Advisory Committee Chairman



---

**Dr. Fred DeJarnette**  
Advisory Committee Member



---

**Dr. Michael Shearer**  
Advisory Committee Minor Representative

# Biography

Jennifer Lou Price was born in Boone, North Carolina on March 11, 1974 to Don E. and Mitzi L. Price. Jennifer spent part of her early years in Gary, Indiana and in Kissimmee, Florida. While living in Florida she was able to watch many Space Shuttle launches and air shows from her back yard, which made a lasting impression on her as a child. She grew up with three younger siblings, Jane, Chris and Jacki. She attended Watauga High School and entered North Carolina State University in the Fall of 1992. She received her Bachelor's of Science in Aerospace Engineering in May of 1999.

In the Fall of 1999 she was awarded a graduate teaching assistantship from the NC State University Department of Mechanical and Aerospace Engineering. She instructed and performed undergraduate aerospace laboratories in the NC State Subsonic Wind Tunnel. In the Spring of 2000 she continued her graduate teaching assistantship where she assisted with the aerospace senior design spacecraft course. In the Fall of 2000 she was awarded a graduate research assistantship for unsteady aerodynamic measurements using hot-film sensors on an oscillating airfoil with Gurney flaps. Jennifer plans on graduating in August 2001 with a Master's Degree in Aerospace Engineering and a minor in Mathematics.

## Acknowledgements

There are so many people who helped make this work possible. First, I would like to thank my advisor, Dr. Ndaona Chokani for his advice, wisdom, support, and encouragement. Thank you especially for all of the opportunities and challenges you have given me. I would also like to thank Dr. Fred DeJarnette and Dr. Michael Shearer for agreeing to be on my graduate committee. Special thanks need to be given to Mr. “Skip” Richardson for the airfoil he spent many hours making and to Mr. Mike Breedlove who helped make the equipment that allowed the experiment to run. In addition, thanks and acknowledgements need to be given to the people of Tao Systems, Inc. for their advice, for the donation and application of the hot-film sensors and for the use of their 16-channel constant voltage anemometer without which the experiment wouldn’t have run. I also would like to thank the North Carolina Super Computing Center, for the hours required for the computations, and the Department of Mechanical and Aerospace Engineering and the North Carolina Space Grant Consortium for their financial support. It also took more than equipment and money to make this happen, it took the advice, support and some “heavy” lifting from my fellow graduate students and friends who I would like to thank, Stearns Heinzen, Warren Jones, Rachel King, and Joe Norris. I would also like to thank Greg Selgrade for all he had to endure and for the support he gave me to help make this happen.

Most importantly, I would like to extend my thanks to my wonderful family. To my Dad and Mom who have loved and supported me unconditionally. Extra special thanks to my loving siblings, Jane, Chris and Jacki as well as all of my grandparents.

# Table of Contents

<b>List of Tables.</b>	. . . . .	<b>.viii</b>
<b>List of Figures.</b>	. . . . .	<b>.ix</b>
<b>List of Symbols.</b>	. . . . .	<b>.xvi</b>
<b>1 Introduction.</b>	. . . . .	<b>.1</b>
<b>1.1 High Lift Aerodynamics/Gurney Flaps.</b>	. . . . .	<b>.1</b>
1.1.1 Applications.	. . . . .	.1
1.1.2 Gurney Flaps.	. . . . .	.1
1.1.3 Previous Experiments on Gurney Flaps.	. . . . .	.1
1.1.4 Previous Computations on Gurney Flaps.	. . . . .	.2
<b>1.2 Unsteady Airfoil Flows.</b>	. . . . .	<b>.3</b>
1.2.1 Features of Unsteady Airfoil Flows.	. . . . .	.3
1.2.2 Previous Experiments on Oscillating Airfoils.	. . . . .	.4
1.2.3 Previous Computations on Oscillating Airfoils.	. . . . .	.5
1.2.4 Control of Dynamic Stall.	. . . . .	.6
<b>1.3 Hot-Film Sensors.</b>	. . . . .	<b>.6</b>
1.3.1 Operating Principle.	. . . . .	.6
1.3.2 Bifurcation Points.	. . . . .	.8
1.3.3 Thermal Anemometry.	. . . . .	.9
<b>1.4 Objectives.</b>	. . . . .	<b>.11</b>

<b>2 Approach.</b>	. . . . .	<b>.12</b>
<b>2.1 Experimental Set-Up.</b>	. . . . .	<b>.12</b>
2.1.1 Wind Tunnel.	. . . . .	.12
2.1.2 Airfoil Model.	. . . . .	.12
2.1.3 Pitching Mechanism.	. . . . .	.13
2.1.4 Instrumentation.	. . . . .	.13
2.1.4.1 Multi-Element Hot-Film Array.	. . . . .	.14
2.1.4.2 Constant Voltage Anemometer System.	. . . . .	.14
2.1.4.3 Data Acquisition System.	. . . . .	.14
<b>2.2 Experimental Analysis.</b>	. . . . .	<b>.15</b>
2.2.1 Hot-Film Measurements.	. . . . .	.15
2.2.2 Statistical Averages and Feature Extraction.	. . . . .	.15
2.2.2.1 Low-Pass Filtering.	. . . . .	.15
2.2.2.2 Phase.	. . . . .	.16
2.2.2.3 Ensemble-Averages.	. . . . .	.16
<b>2.3 Computational Method.</b>	. . . . .	<b>.16</b>
2.3.1 Flow Solver.	. . . . .	.16
2.3.2 Grid Generation.	. . . . .	.18
2.3.3 Boundary Conditions.	. . . . .	.18
<b>3 Results and Discussion.</b>	. . . . .	<b>.20</b>
<b>3.1 Stationary Airfoil.</b>	. . . . .	<b>.20</b>
3.1.1 Effect of Gurney Flap.	. . . . .	.20
3.1.2 Effect of Reynolds Number.	. . . . .	.21

<b>3.2 Oscillating Airfoil.</b>	. . . . .	<b>.22</b>
3.2.1 Oscillation to $\alpha_{\max}=7.2^\circ$ .	. . . . .	.22
3.2.1.1 Effect of Gurney Flap.	. . . . .	.23
3.2.1.2 Effect of Reynolds Number.	. . . . .	.24
3.2.2 Oscillation to $\alpha_{\max}=14.4^\circ$ .	. . . . .	.25
3.2.2.1 Effect of Gurney Flap.	. . . . .	.26
3.2.2.2 Effect of Reynolds Number.	. . . . .	.27
<b>3.3 Flowfield Computations.</b>	. . . . .	<b>.29</b>
3.3.1 Streamlines and Pressure Contours.	. . . . .	.29
3.3.1.1 No Gurney Flap.	. . . . .	.29
3.3.1.2 Gurney Flaps.	. . . . .	.30
3.3.2 Velocity Contours.	. . . . .	.31
3.3.2.1 No Gurney Flap.	. . . . .	.31
3.3.2.2 Gurney Flaps.	. . . . .	.32
3.3.3 Surface Pressure Coefficient.	. . . . .	.33
3.3.3.1 No Gurney Flap.	. . . . .	.33
3.3.3.2 Gurney Flaps.	. . . . .	.33
3.3.4 Skin Friction Coefficient.	. . . . .	.34
3.3.4.1 No Gurney Flap.	. . . . .	.34
3.3.4.2 Gurney Flaps.	. . . . .	.34
3.3.5 Lift and Drag.	. . . . .	.35
<b>4 Concluding Remarks. .</b>	. . . . .	<b>.36</b>
<b>4.1 Summary of Results.</b>	. . . . .	<b>.36</b>

<b>4.2 Recommendations for Future Work.</b>	. . . . .	<b>.37</b>
<b>5 References.</b>	. . . . .	<b>.38</b>
<b>6 Tables.</b>	. . . . .	<b>.43</b>
<b>7 Figures.</b>	. . . . .	<b>.47</b>
<b>8 Appendices.</b>	. . . . .	<b>.120</b>
<b>8.1 Unigraphics Drawings.</b>	. . . . .	<b>.120</b>
<b>8.2 LabVIEW Program.</b>	. . . . .	<b>.132</b>
<b>8.3 Motor Calibration.</b>	. . . . .	<b>.136</b>

## List of Tables

Table 2.1: Sensor locations and resistances. . . . .	.44
Table 3.1: Stagnation, separation, reattachment and vortex core core locations (in terms of s/c) during pitch-up for airfoil with no Gurney flap and $Re=169,000$ . . . . .	.45
Table 3.2: Stagnation, separation and reattachment locations (in terms of s/c) during pitch-down for airfoil with no Gurney flap and $Re=169,000$ . . . . .	.45
Table 3.3: Vortex separation and reattachment locations (in terms of s/c) during pitch-down for airfoil with no Gurney flap and $Re=169,000$ . . . . .	.45
Table 3.4: Vortex core locations (in terms of s/c) during pitch-down for airfoil with no Gurney flap and $Re=169,000$ . . . . .	.45
Table 3.5: Stagnation, separation, reattachment and vortex core core locations (in terms of s/c) during pitch-up for airfoil with 2.5%c Gurney flap and $Re=169,000$ . . . . .	.46
Table 3.6: Stagnation, separation and reattachment locations (in terms of s/c) during pitch-down for airfoil with 2.5%c Gurney flap and $Re=169,000$ . . . . .	.46
Table 3.7: Vortex separation and reattachment locations (in terms of s/c) during pitch-down for airfoil with 2.5%c Gurney flap and $Re=169,000$ . . . . .	.46
Table 3.8: Vortex core locations (in terms of s/c) during pitch-down for airfoil with 2.5%c Gurney flap and $Re=169,000$ . . . . .	.46

# List of Figures

## Chapter 1: Introduction

Figure 1.1: Illustration of a 2.5% <i>c</i> Gurney flap. . . . .	.48
Figure 1.2: Illustration of flow near a Gurney flap as suggested by Liebeck. (From Liebeck, Ref 1). . . . .	.49
Figure 1.3: (a)Unsteady forces and moments in the three dynamic-stall regimes: $M_\infty=0.3$ , $\kappa=0.10$ , $\alpha=\alpha_o+10^\circ\sin(\omega t)$ . (b) sketches of flow fields during light and deep dynamic Stall. (From McCroskey, Ref. 13). . . . .	.50
Figure 1.4: Sequence of events leading up to dynamic stall. (From Carr, Ref. 14). . . . .	.51
Figure 1.5: Phase reversal illustration. (a) Output voltage as a function of sensor location at five instants in time. (b) Output voltage as a function of time at eight sensor locations. (From Moes et al, Ref. 41). . . . .	.52
Figure 1.6: Circuit diagram of (a) constant current anemometer and (b) constant temperature anemometer. (From Comte-Bellot, Ref. 45). . . . .	.53
Figure 1.7: Circuit diagram of a constant voltage anemometer. (From Sarma, Ref. 47). . . . .	.54

## Chapter 2: Approach

Figure 2.1: <i>NACA0012</i> airfoil model mounted in the wind tunnel. . . . .	.55
Figure 2.2: Stepper motor/driver package located on the top of the wind tunnel test section. . . . .	.56
Figure 2.3: Rotary variable inductance transducer mounted under the wind tunnel test section. . . . .	.56

Figure 2.4: Output from inductance transducer for airfoil with 2.5% chord Gurney flap oscillated for 10 periods to $\alpha=7.2^\circ$ at $Re=192,000$ . (a) unfiltered data and (b) filtered data. . . . .	.57
Figure 2.5: Laboratory PC. The LabVIEW interface that is used to control the motor and obtain the data is shown on the monitor. . . . .	.58
Figure 2.6: Connection pins for the data acquisition board. . . . .	.58
Figure 2.7: Cross-sectional view of the <i>NACA0012</i> airfoil showing hot-film sensor locations. . . . .	.59
Figure 2.8: Close-up drawing of hot-film elements and copper leads. . . . .	.59
Figure 2.9: 16-channel constant voltage anemometer system and auto-zero unit. . . . .	.60
Figure 2.10: IOTech <sup>®</sup> digitizers located beneath wind tunnel. . . . .	.60
Figure 2.11: Frequency response of the digital low-pass filter. . . . .	.61
Figure 2.12: Computational grid at $\alpha=14.4^\circ$ . Grid dimensions 438 $\times$ 100. . . . .	.62

### **Chapter 3: Results and Discussion**

Figure 3.1: Low-pass filtered time traces for sensors 11-19, $\alpha=14.4^\circ$ ; no Gurney flap and $Re=169,000$ . . . . .	.63
Figure 3.2: (a) Phase angle for stationary airfoil with no Gurney flap at $\alpha=14.4^\circ$ $Re=169,000$ between sensor pairs 1-3, 3-5, 5-7, 7-9, 9-11 and 11-13. . . . .	.64
Figure 3.2: (b) Phase angle for stationary airfoil with no Gurney flap at $\alpha=14.4^\circ$ $Re=169,000$ between sensor pairs 13-15, 15-17, 17-19, 19-21, 21-23 and 23-25. .. . . .	.65
Figure 3.2: (c) Phase angle for stationary airfoil with no Gurney flap at $\alpha=14.4^\circ$ $Re=169,000$ between sensor pairs 25-27, 27-29 and 29-31. . . . .	.66
Figure 3.3: Low-pass filtered time traces for sensors 11-19, $\alpha=14.4^\circ$ ; 1.5% <i>c</i> Gurney flap and $Re=169,000$ . . . . .	.67

Figure 3.4: (a) Phase angle for stationary airfoil with 1.5% <i>c</i> Gurney flap at $\alpha=14.4^\circ$ $Re=169,000$ between sensor pairs 1-3, 3-5, 5-7, 7-9, 9-11 and 11-13. . . . .	.68
Figure 3.4: (b) Phase angle for stationary airfoil with 1.5% <i>c</i> Gurney flap at $\alpha=14.4^\circ$ $Re=169,000$ between sensor pairs 13-15, 15-17, 17-19, 19-21, 21-23 and 23-25. .. . . .	.69
Figure 3.4: (c) Phase angle for stationary airfoil with 1.5% <i>c</i> Gurney flap at $\alpha=14.4^\circ$ $Re=169,000$ between sensor pairs 25-27, 27-29 and 29-31. . . . .	.70
Figure 3.5: Low-pass filtered time traces for sensors 11-19, $\alpha=14.4^\circ$ ; 2.5% <i>c</i> Gurney flap and $Re=169,000$ . . . . .	.71
Figure 3.6: (a) Phase angle for stationary airfoil with 2.5% <i>c</i> Gurney flap at $\alpha=14.4^\circ$ $Re=169,000$ between sensor pairs 1-3, 3-5, 5-7, 7-9, 9-11 and 11-13. . . . .	.72
Figure 3.6: (b) Phase angle for stationary airfoil with 2.5% <i>c</i> Gurney flap at $\alpha=14.4^\circ$ $Re=169,000$ between sensor pairs 13-15, 15-17, 17-19, 19-21, 21-23 and 23-25. .. . . .	.73
Figure 3.6: (c) Phase angle for stationary airfoil with 2.5% <i>c</i> Gurney flap at $\alpha=14.4^\circ$ $Re=169,000$ between sensor pairs 25-27, 27-29 and 29-31. . . . .	.74
Figure 3.7: Low-pass filtered time traces for sensors 11-19, $\alpha=14.4^\circ$ ; no Gurney flap and $Re=96,000$ . . . . .	.75
Figure 3.8: (a) Phase angle for stationary airfoil with no Gurney flap at $\alpha=14.4^\circ$ $Re=96,000$ between sensor pairs 1-3, 3-5, 5-7, 7-9, 9-11 and 11-13. . . . .	.76
Figure 3.8: (b) Phase angle for stationary airfoil with no Gurney flap at $\alpha=14.4^\circ$ $Re=96,000$ between sensor pairs 13-15, 15-17, 17-19, 19-21, 21-23 and 23-25. .. . . .	.77
Figure 3.8: (c) Phase angle for stationary airfoil with no Gurney flap at $\alpha=14.4^\circ$ $Re=96,000$ between sensor pairs 25-27, 27-29 and 29-31. . . . .	.78
Figure 3.9: Low-pass filtered time traces for sensors 11-19, $\alpha=14.4^\circ$ ; 2.5% <i>c</i> Gurney flap and $Re=96,000$ . . . . .	.79

Figure 3.10: (a) Phase angle for stationary airfoil with 2.5%c Gurney flap at $\alpha=14.4^\circ$ $Re=96,000$ between sensor pairs 1-3, 3-5, 5-7, 7-9, 9-11 and 11-13. . . . .	.80
Figure 3.10: (b) Phase angle for stationary airfoil with 2.5%c Gurney flap at $\alpha=14.4^\circ$ $Re=96,000$ between sensor pairs 13-15, 15-17, 17-19, 19-21, 21-23 and 23-25. .. . . .	.81
Figure 3.10: (c) Phase angle for stationary airfoil with 2.5%c Gurney flap at $\alpha=14.4^\circ$ $Re=96,000$ between sensor pairs 25-27, 27-29 and 29-31. . . . .	.82
Figure 3.11: Time history signals of CVA outputs for sensors 15 to 30. 2.5%c Gurney flap, $Re=96,000$ , $\alpha_{max}=7.2^\circ$ , $\kappa=0.23$ . Symbols denote loci of inflexion points. . . . .	.83
Figure 3.12: Close-up view of time history signals of CVA outputs for sensors 22 to 25. 2.5%c Gurney flap, $Re=96,000$ , $\alpha_{max}=7.2^\circ$ , $\kappa=0.23$ . Symbols denote loci of inflexion points. . . . .	.84
Figure 3.13: Effect of Gurney flap height on unsteady boundary layer separation and transition during airfoil pitch-up and pitch-down for $\alpha_{max}=7.2^\circ$ and $Re=96,000$ . . . . .	.85
Figure 3.14: Effect of Gurney flap height on unsteady boundary layer separation and transition during airfoil pitch-up and pitch-down for $\alpha_{max}=7.2^\circ$ and $Re=169,000$ . . . . .	.86
Figure 3.15: Effect of Gurney flap height on unsteady boundary layer separation and transition during airfoil pitch-up and pitch-down for $\alpha_{max}=7.2^\circ$ and $Re=192,000$ . . . . .	.87
Figure 3.16: Effect of Reynolds number on unsteady boundary layer separation and transition during airfoil pitch-up and pitch-down for $\alpha_{max}=7.2^\circ$ and no Gurney flap.. . . .	.88
Figure 3.17: Effect of Reynolds number on unsteady boundary layer separation and transition during airfoil pitch-up and pitch-down for $\alpha_{max}=7.2^\circ$ and 1.5%c Gurney flap. . . . .	.89
Figure 3.18: Effect of Reynolds number on unsteady boundary layer separation and transition during airfoil pitch-up and pitch-down for $\alpha_{max}=7.2^\circ$ and 2.5%c Gurney flap. . . . .	.90

Figure 3.19: Time history signals of CVA outputs for sensors 15 to 30. 2.5% c Gurney flap, $Re=96,000$ , $\alpha_{max}=14.4^\circ$ , $\kappa=0.23$ . Symbols denote loci of inflexion points. . . . .	.91
Figure 3.20: Close-up view of time history signals of CVA outputs for sensors 22 to 25. 2.5% c Gurney flap, $Re=96,000$ , $\alpha_{max}=14.4^\circ$ , $\kappa=0.23$ . Symbols denote loci of inflexion points. . . . .	.92
Figure 3.21: Effect of Gurney flap height on unsteady boundary layer separation and transition during airfoil pitch-up for $\alpha_{max}=14.4^\circ$ and $Re=96,000$ . . . . .	.93
Figure 3.22: Effect of Gurney flap height on unsteady boundary layer separation and transition during airfoil pitch-up for $\alpha_{max}=14.4^\circ$ and $Re=169,000$ . . . . .	.94
Figure 3.23: Effect of Gurney flap height on unsteady boundary layer separation and transition during airfoil pitch-up for $\alpha_{max}=14.4^\circ$ and $Re=192,000$ . . . . .	.95
Figure 3.24: Effect of Gurney flap height on unsteady boundary layer separation, transition and reattachment during airfoil pitch-down for $\alpha_{max}=14.4^\circ$ and $Re=96,000$ . . . . .	.96
Figure 3.25: Effect of Gurney flap height on unsteady boundary layer separation, transition and reattachment during airfoil pitch-down for $\alpha_{max}=14.4^\circ$ and $Re=169,000$ . . . . .	.97
Figure 3.26: Effect of Gurney flap height on unsteady boundary layer separation, transition and reattachment during airfoil pitch-down for $\alpha_{max}=14.4^\circ$ and $Re=192,000$ . . . . .	.98
Figure 3.27: Effect of Reynolds number on unsteady boundary layer separation and transition during airfoil pitch-up for $\alpha_{max}=14.4^\circ$ and no Gurney flap. . . . .	.99
Figure 3.28: Effect of Reynolds number on unsteady boundary layer separation and transition during airfoil pitch-up for $\alpha_{max}=14.4^\circ$ and 1.5% c Gurney flap. . . . .	.100
Figure 3.29: Effect of Reynolds number on unsteady boundary layer separation and transition during airfoil pitch-up for $\alpha_{max}=14.4^\circ$ and 2.5% c Gurney flap. . . . .	.101

Figure 3.30: Effect of Reynolds number on unsteady boundary layer separation, transition and reattachment during airfoil pitch-down for $\alpha_{\max}=14.4^\circ$ and no Gurney flap. . . . .	.102
Figure 3.31: Effect of Reynolds number on unsteady boundary layer separation, transition and reattachment during airfoil pitch-down for $\alpha_{\max}=14.4^\circ$ and 1.5%c Gurney flap. . . . .	.103
Figure 3.32: Effect of Reynolds number on unsteady boundary layer separation, transition and reattachment during airfoil pitch-down for $\alpha_{\max}=14.4^\circ$ and 2.5%c Gurney flap. . . . .	.104
Figure 3.33: Streamlines and pressure contours for airfoil with no Gurney flap during pitch-up at $Re=169,000$ . (a) $2.4^\circ$ (b) $4.8^\circ$ (c) $7.2^\circ$ (d) $9.6^\circ$ (e) $12.0^\circ$ and (f) $14.4^\circ$ . . . . .	.105
Figure 3.34: Streamlines and pressure contours for airfoil with no Gurney flap during pitch-down at $Re=169,000$ . (a) $12.0^\circ$ (b) $9.6^\circ$ (c) $7.2^\circ$ (d) $4.8^\circ$ (e) $2.4^\circ$ and (f) $0.0^\circ$ . . . . .	.106
Figure 3.35: Streamlines and pressure contours for airfoil with 2.5%c Gurney flap during pitch-up at $Re=169,000$ . (a) $2.4^\circ$ (b) $4.8^\circ$ (c) $7.2^\circ$ (d) $9.6^\circ$ (e) $12.0^\circ$ and (f) $14.4^\circ$ . . . . .	.107
Figure 3.36: Streamlines and pressure contours for airfoil with 2.5%c Gurney flap during pitch-down at $Re=169,000$ . (a) $12.0^\circ$ (b) $9.6^\circ$ (c) $7.2^\circ$ (d) $4.8^\circ$ (e) $2.4^\circ$ and (f) $0.0^\circ$ . . . . .	.108
Figure 3.37: Experimental and computational separation locations for both the clean and 2.5%c Gurney flap airfoil during pitch-up to $\alpha=14.4^\circ$ at $Re=169,000$ . . . . .	.109
Figure 3.38: Experimental and computational separation and reattachment locations for both the clean and 2.5%c Gurney flap airfoil during pitch-down to $\alpha=14.4^\circ$ at $Re=169,000$ . . . . .	.110
Figure 3.39: Velocity contours for airfoil with no Gurney flap during pitch-up at $Re=169,000$ . (a) $2.4^\circ$ (b) $4.8^\circ$ (c) $7.2^\circ$ (d) $9.6^\circ$ (e) $12.0^\circ$ and (f) $14.4^\circ$ . . . . .	.111
Figure 3.40: Velocity contours for airfoil with no Gurney flap during pitch-down at $Re=169,000$ . (a) $12.0^\circ$ (b) $9.6^\circ$ (c) $7.2^\circ$ (d) $4.8^\circ$ (e) $2.4^\circ$ and (f) $0.0^\circ$ . . . . .	.112

Figure 3.41: Velocity contours for airfoil with 2.5%c Gurney flap during pitch-up at Re=169,000. (a) 2.4° (b) 4.8° (c) 7.2° (d) 9.6° (e) 12.0° and (f) 14.4° . . . . .	.113
Figure 3.42: Velocity contours for airfoil with 2.5%c Gurney flap during pitch-down at Re=169,000 (a) 12.0° (b) 9.6° (c) 7.2° (d) 4.8° (e) 2.4° and (f) 0.0° . . . . .	.114
Figure 3.43: Pressure coefficient versus chord location for airfoil with no Gurney flap at Re=169,000. (a) pitch-up and (b) pitch-down. . . . .	.115
Figure 3.44: Pressure coefficient versus chord location for airfoil with 2.5%c Gurney flap at Re=169,000. (a) pitch-up and (b) pitch-down. . . . .	.116
Figure 3.45: Skin friction coefficient versus chord location for airfoil with no Gurney flap at Re=169,000. (a) pitch-up and (b) pitch-down. . . . .	.117
Figure 3.46: Skin friction coefficient versus chord location for airfoil with 2.5%c Gurney flap at Re=169,000. (a) pitch-up and (b) pitch-down. . . . .	.118
Figure 3.47: Lift and drag coefficient hysteresis plots for airfoil at Re=169,000. (a) $C_l$ versus $\alpha$ (b) $C_d$ versus $\alpha$ . . . . .	.119

# List of Symbols

## Roman Symbols

$a_s$	overheat ratio
$c$	airfoil chord
$C_D, C_d$	drag coefficient
$C_L, C_l$	lift coefficient
$C_M$	pitching moment coefficient
$\hat{D}$	vector of conserved terms
$e$	convective terms in Navier-Stokes equation
$e_v$	viscous flux term in Navier-Stokes equation
$\hat{E}$	vector of convective terms
$\hat{E}_v$	vector of viscous forces
$f$	convective term in Navier-Stokes equation
$f_v$	viscous flux term in Navier-Stokes equation
$f$	oscillation frequency
$\hat{F}$	vector of convective terms
$\hat{F}_v$	vector of viscous forces
$f_n$	Nyquist frequency
$f_p$	filter bandwidth
$f_t$	filter transition gap
$i$	fluctuation in current
$I$	current
$J$	Jacobian
$p$	pressure
$Q_f$	heat loss to substrate
$r$	fluctuation in resistance
$R$	resistance
$Re$	Reynolds number based on airfoil chord
$s$	surface distance
$S$	sensor
$t$	time
$T_a$	ambient temperature
$T_s$	sensor temperature
$u$	x-component of velocity
$U_\infty$	freestream velocity
$v$	fluctuation in voltage, y-component of velocity
$V$	voltage
$x$	chordwise distance

## Greek Symbols

$\alpha$	angle of attack
$\beta$	artificial compressibility term
$\phi$	phase angle
$\eta$	x-transformation coordinate
$\kappa$	reduced frequency, $\pi fc/U_\infty$
$\tau$	pseudo-time
$\tau_w$	wall shear stress
$\omega$	frequency, $2\pi f$
$\xi$	y-transformation coordinate

## Abbreviations

CCA	constant current anemometer
CTA	constant temperature anemometer
CVA	constant voltage anemometer
GF	Gurney flap
IP	inflection point

## Subscripts

a	ambient
max	maximum
s	sensor
w	wire
$\infty$	freestream conditions

## Superscripts

—	mean
$\wedge$	vector

# Chapter 1

## Introduction

### 1.1 High Lift Aerodynamics/Gurney Flaps

#### 1.1.1 Applications

Dan Gurney first used Gurney flaps with the objective of creating more downforce on racecars. Later Liebeck<sup>1</sup> suggested the use of the Gurney flaps for aircraft applications. Modified trailing edges, such as divergent trailing edges, are now used on commercial transport aircraft for improved performance at transonic cruise conditions.<sup>2</sup>

#### 1.1.2 Gurney Flaps

The Gurney flap is a short strip that is fitted perpendicular to the pressure surface along the trailing edge of an airfoil, Fig. 1.1. Liebeck,<sup>1</sup> Giguère et al,<sup>3</sup> and Myose et al<sup>4</sup> provide reviews of the effects of Gurney flaps on the aerodynamics of airfoils. These effects include: the increase in the maximum lift coefficient, the decrease in the angle of attack for zero lift while the slope of the lift curve remains relatively constant, and the increase in the nose-down pitching moment. The flap has a typical size of 1-5% of the chord. This flap increases the lift and decreases the drag when its height is less than 2% of the chord. An increase in height beyond 2% of the chord yields an increase in lift that is obtained at the cost of substantially increased drag.

#### 1.1.3 Previous Experiments on Gurney Flaps

Neuhart and Pendergraft<sup>5</sup> conducted flow visualization tests of the flow field near a Gurney flap. The tests were conducted in a water tunnel, and showed that the time-averaged flow behind the Gurney flap consists of two-counter-rotating vortices. This

flowfield was first proposed by Liebeck<sup>1</sup>, Fig. 1.2. More recently Jeffery et al<sup>6</sup> conducted laser Doppler anemometry (LDA) measurements downstream of a Gurney flap. The LDA data show that the wake consists of a von Kármán vortex sheet of alternately shed vortices. The vortex shedding increases the suction at the trailing edge on the suction side of the airfoil; on the pressure side of the airfoil the Gurney flap decelerates the flow and thus increases the pressure. The pressure difference that results across the trailing edge generates the increase in the airfoil's circulation. Bloy and Durant<sup>7</sup> examined the effects of different flap shapes. They found that the performance of an airfoil with a 45° trailing-edge flap is superior to the same airfoil with a similarly sized Gurney flap. Storms and Jang<sup>8</sup> obtained the pressure distributions and wake profiles on an airfoil equipped with Gurney flaps. They observed that at high lift coefficients there was less drag, but more drag resulted at low to moderate lift coefficients.

#### **1.1.4 Previous Computations on Gurney Flaps**

Jang et al<sup>9</sup> used the incompressible Navier-Stokes code INS2D to calculate the flow field about an airfoil equipped with a Gurney flap. The computational results showed that the flow field structure in the vicinity of the Gurney flap was close to the model proposed by Liebeck.<sup>1</sup> Ross et al<sup>10</sup> conducted an experimental and computational study on the use of Gurney flaps on two-element airfoils. The INS2D code with the Baldwin-Barth turbulence model was used. The predicted pressure distributions showed very good agreement with the experiment. Carrannanto et al<sup>11</sup> also used the INS2D code to analyze the effectiveness of Gurney flaps on two- and three-element airfoils. The Gurney flap was observed to be effective in improving the maximum lift and lift-to-drag ratio relative to an airfoil without the Gurney flap. Janus<sup>12</sup> used a Navier-Stokes solver to

investigate the effect of Gurney flaps on the performance of industrial fan blades. A Gurney flap size of 1-1.5% chord was observed to provide the best performance of the fan blades.

## **1.2 Unsteady Airfoil Flows**

### **1.2.1 Features of Unsteady Airfoil Flows**

The unsteady flow past an airfoil has been the subject of comprehensive reviews and surveys presented by McCroskey,<sup>13</sup> Carr,<sup>14</sup> Carr and McCroskey<sup>15</sup> and Carr and Chandrasekhara.<sup>16</sup> When the airfoil pitches through the static-stall angle of attack to higher angles of attack, the unsteady boundary layer separates and dynamic stall phenomena occur. The maximum angle of attack for sinusoidal oscillations is the primary parameter that determines the degree of flow separation. *Light* dynamic stall, Fig. 1.3, has a separated flow region whose vertical extent is of the order of the airfoil thickness. In this case  $\alpha_{\max}$  is only slightly greater than the static-stall angle. *Deep* dynamic stall occurs when the maximum incidence is well in excess of the static-stall angle. The sequence of events leading up to the deep dynamic stall is illustrated in Figure 1.4. It begins with boundary layer reversal, which is indicated by a reversed flow region associated with a separated shear layer. Also, as the airfoil pitches upwards the boundary layer transition point moves forward on the airfoil. Depending on the flow parameters the boundary layer may reattach to the airfoil. Once the angle of attack is greater than the static-stall angle the separated unsteady boundary layer forms a leading edge vortex. This vortex grows in size and strength before it is convected downstream at a constant velocity and is subsequently shed into the airfoil's wake. This shedding cause a brief, but

substantial, increase in lift followed by a potentially catastrophic stall. During the vortex shedding the thickness of the viscous layer is of the order of the airfoil chord.

### **1.2.2 Previous Experiments on Oscillating Airfoils**

In addition to knowledge of the large-scale unsteady flowfield features, it is necessary to characterize the unsteady boundary layer events that give rise to the dynamic stall phenomena. Carr et al<sup>17</sup> identified three different types of unsteady boundary layer reversal that lead to dynamic stall on a pitching airfoil. The unsteady boundary layer transition and relaminarization on a pitching wing has been characterized by Lorber and Carta.<sup>18</sup> They used simultaneous hot-film sensor and pressure measurements to show that for high Reynolds numbers, greater than  $2 \times 10^6$ , transition occurs before the separation, and thus the appearance of a laminar separation bubble is averted. The effects of compressibility, sweep, pitch-rate and proximity to the wing tip on the transition and relaminarization locations were examined. Schreck et al<sup>19</sup> examined the effect of pitch rate and Reynolds number on the unsteady boundary layer during the pitch-up of an airfoil. Hot-film sensor data was used to show that the unsteady boundary layer reversal was delayed to higher angles of attack as the pitch rate was elevated. Lee and Basu<sup>20</sup> examined the progression of the laminar separation, transition and turbulent reattachment on an airfoil that is oscillated within and beyond static stall. The hot-film sensor data for this study show that the laminar separation point and transition were delayed with increasing angle of attack and that reattachment and relaminarization were promoted compared with the static cases. It was also suggested that the dynamic stall process was initiated by turbulent flow separation at the leading edge and flow reversal near the trailing edge. Carr et al,<sup>21</sup> Ahmed and Chandrasekhara,<sup>22</sup> and Chandrasekhara et al<sup>23</sup>

have performed flow visualization studies to study dynamic stall and the flow phenomena for an oscillating airfoil. Carr et al<sup>21</sup> used real-time interferometry, similar to the Schlieren method, to study dynamic stall during pitch-up. Ahmed and Chandrasekhara<sup>22</sup> used stroboscopic Schlieren, two-component laser Doppler velocimetry and point diffraction interferometry to study the reattachment process on an airfoil during pitch-down. Chandrasekhara et al<sup>23</sup> studied the effect of two competing mechanisms, supersonic flow and bubble dynamics, on dynamic stall onset using point diffraction interferometry. These studies suggest that bubble bursting is the cause of dynamic stall for low and moderate Reynolds numbers. As the Mach number is increased an interaction between the supersonic flow and the bubble initiates the dynamic stall and at even higher Mach numbers the shock-induced boundary layer separation causes the dynamic stall.

### **1.2.3 Previous Computations on Oscillating Airfoils**

Aso and Hayashi<sup>24</sup> investigated the dynamic stall phenomena using two different numerical methods: a discrete vortex method and an incompressible Navier-Stokes solver. The discrete vortex method combined a panel method with an integral boundary layer code. Both methods were capable of simulating the separated flows around an airfoil. Ko and McCroskey<sup>25</sup> computed the unsteady separated turbulent flows on an oscillating *NACA0015* airfoil using a thin-layer Navier-Stokes code. Three different turbulence models were used, and flow conditions corresponding to attached flows, light dynamic stall and deep dynamic stall were examined. Two turbulent flows over an oscillating *NACA0012* airfoil were computed by Badcock et al.<sup>26</sup> A pseudo time formulation of the Reynolds-Averaged Navier-Stokes equation was used in their numerical method, and yielded results that were in good agreement with the experiment.

#### **1.2.4 Control of Dynamic Stall**

Several methods have been previously examined to manage and control the adverse effects of dynamic stall. These methods may be separated into two categories: boundary layer control and modifications to the airfoil geometry. In the first category some examples include suction, steady and pulsed blowing, and periodic excitation. Karim and Acharya<sup>27</sup> and Alrefai and Acharya<sup>28</sup> showed that leading-edge suction was effective in controlling the reverse-flow accumulation, and thus delayed the formation of the dynamic stall vortex. Weaver et al<sup>29</sup> found that steady upper surface blowing was capable of trapping the leading edge separation bubble, and thus averting stall. For their test conditions pulsed blowing was not observed to be as effective as steady blowing. Greenblatt and Wygnanski<sup>30</sup> and Greenblatt et al<sup>31</sup> have observed that both light and deep stall can be controlled using periodic excitation – that is alternate blowing and suction. They also observed that the periodic excitation was superior to steady blowing. In the second category the concepts that have been considered include a leading-edge slat, a drooped leading edge and a deformable leading edge. Yu et al<sup>32</sup> and Carr et al<sup>33</sup> have shown that a multi-element airfoil, that consists of a slat and main element, can operate well into post-stall areas without the occurrence of a dynamic stall vortex. Yu et al<sup>32</sup> observed that the lift hysteresis could be substantially decreased by drooping the leading edge during a pitch-oscillation. Chandrasekhara et al<sup>34</sup> have demonstrated that the dynamic stall vortex can be avoided by dynamically changing the leading edge shape during oscillation.

### **1.3 Hot-Film Sensors**

#### **1.3.1 Operating Principle**

Hanratty and Campbell<sup>35</sup> have recently reviewed the various techniques available to measure the wall shear stress. One principal technique is the use of a flush-mounted, thin, metallic element that is resistively heated to a temperature above that of the surrounding fluid. Fage and Falkner<sup>36</sup> first studied the use of heated elements to determine the skin friction in incompressible laminar flows. Ludwig,<sup>37</sup> who considered a heated element submerged in a viscous sublayer, pioneered the measurement in the turbulent case. Liepmann and Skinner<sup>38</sup> studied both laminar and turbulent flows over a flat plate; small hot-wires embedded in an insulating surface were used to measure the local skin-friction. They also showed, by dimensional analysis, that the heat loss from the wire is proportional to the cube root of the wall shear stress. Bellhouse and Schultz<sup>39</sup> measured the mean skin friction in laminar and turbulent flows on a flat plate, circular cylinder and in an annular tunnel. They observed that a sharp increase in the mean current could be used to indicate transition, and a minimum in the current indicates laminar separation. Menendez and Ramaprian<sup>40</sup> developed the relevant formula for the use of hot-films in unsteady laminar and turbulent flows. The accuracy of the formula was verified by comparison against the exact numerical solutions of thermal and hydrodynamic boundary layers.

The operation of flush-mounted hot-film sensors is based on the fact that the heat transfer from a sufficiently small heated surface depends only on the flow characteristics in the viscous sublayer region of the boundary layer. During its operation, the hot-film sensor is resistively heated to a temperature that is greater than the fluid temperature, as defined by the overheat ratio:

$$a_s = \frac{T_s - T_a}{T_a} \quad (1)$$

Since the sensor has a temperature-dependent resistance:

$$R_s = R_r [ 1 + \alpha ( T_s - T_r ) ] \quad (2)$$

as its' temperature varies with changes in the flow environment, so does its' resistance, and hence the Joulean heating rate. The convection of heat from the sensor is related to the wall shear stress according to the classical relation first presented by Ludwig:<sup>37</sup>

$$\tau_w \sim Q_f^3 \quad (3)$$

In this relation the conductive heat loss to the substrate is neglected, although depending on the material of the substrate this might have an important effect, Cook.<sup>41</sup> However, this is only significant if a calibration of the hot-films is required.

### 1.3.2 Bifurcation Points

Stack et al<sup>42,43</sup> observed that in the presence of flow bifurcation, where the convective heat transfer is a minimum, a 180° phase shift phenomenon occurs. This phase shift reversal is illustrated in Figure 1.5,<sup>44</sup> where the hypothetical voltages output from eight hot-film sensors, at five successive instants in time, are graphed. At the initial time, t1, the bifurcation point is located at sensor S4. As the time changes the bifurcation moves to sensor S5 at time t2, sensor S4 at time t3, sensor S3 at time t4, and lastly sensor S4 at time t5. The corresponding time histories show that the group of sensors S1, S2 and S3 are in-phase with each other; the group of sensors S5, S6, S7 and S8 are in-phase with each other, but 180° out-of-phase with the first group of sensors. In addition it can be seen that at sensor S4, which is the time-mean location of the bifurcation point, the voltage varies at twice the frequency of the other sensors. Thus in the presence of a flow

bifurcation that is associated with a minimum in the convective heat transfer (and skin friction), there is:

- i) a  $180^\circ$  phase reversal between the sensors on either side of the bifurcation point; and
- ii) a frequency at the bifurcation point that is twice the frequency at other locations.

### 1.3.3 Thermal Anemometry

Comte-Bellot<sup>45</sup> provides a recent review of thermal anemometry. Two types of anemometers have traditionally been used in thermal anemometry to provide the Joulean or resistive heating to hot-wire/hot-film sensors: constant current and constant temperature. In the constant current anemometer (CCA), Fig. 1.6(a), the sensor resistance caused by variations in the convective heat transfer is measured as a drop across the sensor. In the constant temperature anemometer (CTA), Fig. 1.6(b), a feedback loop is used to maintain the temperature (and resistance) of the sensor constant. The variations in the heat transfer produce fluctuations in the current through the sensor. Although the CCA and CTA have been widely used in many flows, they have deficiencies with respect to sensitivities and signal-to-noise. The constant voltage anemometer (CVA) was thus developed by Sarma<sup>46</sup> address these deficiencies, Fig. 1.7. The particular attributes of the CVA include its high sensitivity, large bandwidth, low noise and easy operational use.

Sarma<sup>47,48</sup> presents and analyzes the electronic circuit of the CVA. Its three basic elements are a) a stable, low-noise, DC power supply; b) an operational amplifier (op-amp); and c) a T-resistor network. The non-inverting terminal of the op-amp is grounded, and for the output of the op-amp to be finite, the differential input must be

equal to zero. Thus  $V_i=0$ , and an application of Kirchoff's current law to the inverting terminal of the op-amp gives

$$V_w = -V_1 \frac{R_F}{R_1} \quad (4)$$

Since  $R_F$  and  $R_1$  are passive resistances, equation (4) provides a constant voltage across the sensor,  $R_w$ , and thus the constant voltage characteristic of the CVA. The changes in the sensor resistance, caused by variations in the convective heat transfer from the sensor, result in fluctuations in the sensor current

$$V_w = I_w R_w = (\overline{I_w} + i_w)(\overline{R_w} + r_w) = \overline{I_w} \overline{R_w} + i_w \overline{R_w} + r_w \overline{I_w} \quad (5)$$

In equation (5) the quadratics in the fluctuations are considered negligible. Since the sensor voltage is a constant, equation (5) then gives:

$$i_w \overline{R_w} = -r_w \overline{I_w} \quad (6)$$

Kirchoff's current law can also be applied to the center node of the T-resistor to give:

$$\frac{V_w}{R_F} + \frac{V_w}{R_w} + \frac{V_w - V_s}{R_2} = 0 \quad (7)$$

The output voltage of the CVA can be obtained by rearranging equation (7):

$$V_s = I_w R_2 + \frac{R_F + R_2}{R_F} V_w \quad (8)$$

If we now consider changes in the output voltage,  $V_s = \overline{V_s} + v_s$ , and fluctuations in the sensor current,  $I_w = \overline{I_w} + i_w$ , equations (6) and (8) combine to give:

$$v_s = -\overline{I_w} R_2 \frac{r_w}{R_w} \quad (9)$$

This output voltage is analyzed to obtain the locations of flow bifurcation in the present experiment.

#### **1.4 Objectives**

Although we have some detailed knowledge of the aerodynamic performance and flowfield characteristics of an airfoil fitted with a Gurney flap, all the previous experimental and computational studies have been with the airfoil in an oncoming steady flow. In practice, the operating environment includes unsteady conditions that may be due to vehicle dynamics (for example a phugoid or pitching motion), vehicle aerodynamics (for example wing-strut flow interaction) or the environment (for example gusts). It is thus of interest to examine the fluid physics of an airfoil fitted with a Gurney flap in an unsteady flow. Thus the objective of the present work is to examine the effect of the Gurney flap on the flow phenomena on the upper surface of an airfoil that is oscillated within and slightly beyond the static-stall angle of attack.

The present work is both experimental and computational in nature. In the experiments, a wind tunnel study of an unsteady airfoil equipped with a Gurney flap is conducted. The locations of stagnation, separation and reattachment points, and transition-to-turbulence are determined using multiple hot-film sensors operated by a CVA. These measurements are limited to the airfoil's surface. Thus a parallel computational study is also conducted using the INS2D code to document the off-surface flow features, and correlate these with the experimental measurements.

# Chapter 2

## Approach

### 2.1 Experimental Set-Up

#### 2.1.1 Wind Tunnel

The experiment was conducted in the NC State University Subsonic Wind Tunnel. The tunnel is of the closed-loop type and has a test section with dimensions of  $0.81m$  in height,  $1.14m$  in width and  $1.17m$  in length. Upstream of the contraction section are turbulence-reduction devices consisting of a honeycomb followed by stainless steel mesh. Tunnel calibration indicates that the freestream turbulence levels are less than 0.33%. The tunnel speed can be continuously varied to a maximum speed of  $40m/s$  at a dynamic pressure of  $720Pa$ .

#### 2.1.2 Airfoil Model

The airfoil model for the experiments is made out of stock aluminum. The airfoil section is a *NACA0012*. The coordinates for the airfoil section were obtained from XFOIL<sup>®</sup>, a panel method that is based on the linear-vorticity stream function.<sup>49</sup> The graphics package Unigraphics<sup>®</sup> was then used to generate the airfoil coordinates at every  $0.001in$ . The span of the finished model is  $76.2cm$  and has a  $15.24cm$  chord. The model is vertically mounted in the center of the wind tunnel test section, Figure 2.1. Two different Gurney flap heights of 1.5 and 2.5% chord are tested. The flaps are made out of  $0.6mm$  thick stainless steel sheet, which is bent to a  $90^\circ$  angle. One face of the sheet is

then attached to the airfoil model using 0.0381mm double-sided tape. The specifications for the experimental set-up can be found in Appendix 8.1.

### 2.1.3 Pitching Mechanism

A *Super Vexta*<sup>®</sup> 5-phase UPD5913H-NAA stepper motor and driver package that is mounted on top of the tunnel test-section is used to oscillate the airfoil about the quarter chord location, Fig. 2.2. The minimum step angle of the motor is 0.72° with 500 full steps (pulses) per revolution. The motor driver accepts four signals, which are low level, TTL, step and direction signals. The “on” or “high” voltage is in the range of 4-5V and the “off” or “low” voltage is in the range of 0-0.5V.

The angle of attack is simultaneously read with a Schaevitz<sup>®</sup> RVIT-15-60 rotary variable inductance transducer that is mounted below the tunnel test section, Fig 2.3. Figure 2.4 shows example plots of output from the transducer.

The laboratory PC used for the motor control is a Gateway<sup>®</sup> P5-120 with a 120MHz Pentium<sup>®</sup> Processor and 320MB RAM, Fig. 2.5. The motor is controlled through LabVIEW<sup>®</sup> via a National Instruments<sup>™</sup> AT-MIO-16F-5 data acquisition (DAQ) board. This DAQ board has analog, digital, and timing I/O that are PC compatible. It has a 5ms, 12-bit sampling capability, and 16 single-ended or 8 differential channels. The three independent 16-bit counter/timers for frequency counting, event counting, and pulse output applications are used in the present work. Figure 2.6 shows the motor wiring to the connection pins for the DAQ board. Further details of the motor calibration and information about the LabVIEW<sup>®</sup> program can be found in Sections 8.2 and 8.3 respectively.

### 2.1.4 Instrumentation

#### **2.1.4.1 Multi-Element Hot-Film Array**

The airfoil is equipped with an array of surface-mounted, hot-film sensors. The sensor array is oriented along a streamwise row at the quarter-span of the airfoil, as seen in Figure 2.1. The array of 32 sensors are electron beam deposited,  $2.54mm$  apart, onto a  $50\text{-micron}$  thick Kapton sheet that is placed on the forward 25% chord on the airfoil's upper and lower surfaces, Fig. 2.7. The sensor numbers, locations and resistances are listed in Table 2.1. Each nickel sensor element is  $1.65mm$  long (spanwise direction),  $0.13mm$  wide (streamwise direction) and  $0.3\text{micron}$  thick, Fig. 2.8. Copper leads of thickness  $0.0127mm$  and width  $0.762mm$  are used to connect the sensors to the anemometer system.

#### **2.1.4.2 Constant Voltage Anemometer System**

The sensors are operated using a 16-channel constant voltage anemometry (CVA) system,<sup>48</sup> Fig. 2.9. The anemometer bandwidths, as determined using the square wave test, are  $250kHz$ . However the response of the sensors in an unsteady flow is limited to frequencies up to no more than  $200Hz$  due to the presence of the Kapton substrate; this is sufficient for the present experiment. The CVA system used also has an auto-zero feature, which allows the user to remove the heat conduction losses to the substrate and thus obtain the signal for only the heat that is convected to the flow.

#### **2.1.4.3 Data Acquisition System**

The data was obtained using two IOTech<sup>®</sup> WaveBook/512<sup>™</sup> portable digitizers, Fig. 2.10. The WaveBook<sup>™</sup> system is used to measure the dynamic hot-film sensor signals. Each digitizer is capable of 12-bit resolution on eight differential inputs, at up to  $1MHz$ . The WaveBooks<sup>™</sup> are connected to a PC via an enhanced parallel port. The PC used in

the data acquisition is a Gateway<sup>®</sup> with an 800MHz Pentium<sup>®</sup> Processor. WaveView,<sup>™</sup> the Windows<sup>®</sup>-based graphical data acquisition and display software included with the WaveBook<sup>™</sup> system is used to display and store the continuous data signals as they are obtained.

## **2.2 Experimental Analysis**

The experiments were performed for both stationary and oscillating airfoil cases. The maximum angles of attack are  $7.2^\circ$  and  $14.4^\circ$ . The experiments are conducted at speeds of 9.2, 16.2 and 18.4m/s, that yield Reynolds numbers based on the airfoil chord of 96,000, 169,000 and 192,000, and reduced frequencies of 0.23, 0.13 and 0.12, respectively. These conditions are comparable to those of Schreck et al<sup>19</sup> and Lee et al.<sup>20</sup> During the oscillations the minimum angle of attack is  $0^\circ$  and the oscillation frequency is 4.5Hz; thus the corresponding pitch rates are 65.45<sup>o</sup>/s and 130.9<sup>o</sup>/s, respectively for the oscillating airfoil.

### **2.2.1 Hot-Film Measurements**

Every other sensor on the upper and lower surfaces is examined for the stationary airfoil cases. In the case of the oscillating airfoil only the sensors on the upper surface are examined; that is from sensor 15 at the leading edge to sensor 30, which is at  $s/c=0.25$  chord, Fig. 2.7. All of the data are obtained at a sampling frequency of 2kHz with a 12-bit resolution.

### **2.2.2 Statistical Averages and Feature Extraction**

#### **2.2.2.1 Low-Pass Filtering**

For the stationary airfoil, a low-pass digital filter<sup>50</sup> was applied to the data obtained with the CVA, Fig. 2.11. This filter was flat over a bandwidth of 250Hz. The

purpose of this filtering was to more clearly observe the  $180^\circ$  phase difference across the stagnation and separation points.<sup>43</sup>

#### **2.2.2.2 Phase**

The  $180^\circ$  phase reversals between the sensors were determined from the cross-spectral densities calculated using a MATLAB<sup>®</sup> program. The cross-spectral densities were obtained for all adjacent pairs of sensors. If a  $180^\circ$  phase reversal exists then the location of stagnation or separation points between the sensors can be determined.

#### **2.2.2.3 Ensemble-Averages**

Since the oscillating airfoil data are not statistically stationary, the  $180^\circ$  phase reversal phenomena obtained from the cross-spectral densities cannot be used to identify the bifurcation points. For the oscillating airfoil ensemble-averaged time histories are computed using 10 oscillation periods. The ensemble-averaged time histories are then examined to identify the locations of boundary layer separation, transition and reattachment. The boundary layer separation and reattachment locations are identified from a local minimum in the voltage time histories. The boundary layer transition locations are determined from an increase in the standard deviation of the signal. Transition to a fully turbulent flow is identified from a maximum in the voltage signal.

### **2.3 Computational Method**

#### **2.3.1 Flow Solver**

In parallel with the experiment a series of Reynolds-averaged Navier-Stokes computations were conducted on the NC Supercomputing Center's Cray T-90 supercomputer. The incompressible Navier-Stokes code INS2D-UP, developed at NASA Ames Research Center, is employed. This code is more fully described by Rogers and

Kwak<sup>51</sup> but a few of its salient features are presented here for completeness. The unsteady two-dimensional equations are solved in generalized coordinates for steady or unsteady flows. The conservation form of the equations may be expressed as:

$$\frac{\partial}{\partial \mathbf{x}} \left( \frac{U}{J} \right) + \frac{\partial}{\partial \mathbf{h}} \left( \frac{V}{J} \right) = 0 \quad (1)$$

$$\frac{\partial \hat{u}}{\partial t} = - \frac{\partial}{\partial \mathbf{x}} (\hat{e} - \hat{e}_v) - \frac{\partial}{\partial \mathbf{h}} (\hat{f} - \hat{f}_v) \quad (2)$$

The method of artificial compressibility is used to couple the continuity equation, (1), with the momentum equation, (2). In this method a time derivative of pressure is added to the continuity equation:

$$\frac{\partial p}{\partial t} = - \mathbf{b} \nabla \cdot \hat{u} \quad (3)$$

The equations (2) and (3) can be iterated in time for a steady-state flow to yield a converged solution. For unsteady flows a pseudo-time derivative is added to both equations (2) and (3).

$$\frac{\partial \hat{D}}{\partial t} = - \frac{\partial \hat{D}}{\partial t} - \frac{\partial}{\partial \mathbf{x}} (\hat{E} - \hat{E}_v) - \frac{\partial}{\partial \mathbf{h}} (\hat{F} - \hat{F}_v) \quad (4)$$

where,

$$\hat{D} = \frac{1}{J} \begin{bmatrix} p \\ u \\ v \end{bmatrix} \quad \hat{E} = \frac{1}{J} \begin{bmatrix} \mathbf{b} U \\ \mathbf{x}_x p + uU + \mathbf{x}_t u \\ \mathbf{x}_y p + vU + \mathbf{x}_t v \end{bmatrix} \quad (5a)$$

$$\hat{F} = \frac{1}{J} \begin{bmatrix} \mathbf{b} U \\ \mathbf{h}_x p + uV + \mathbf{h}_t u \\ \mathbf{h}_y p + vV + \mathbf{h}_t v \end{bmatrix} \quad \hat{E}_v = \begin{bmatrix} 0 \\ \hat{e}_v \end{bmatrix} \quad \hat{F}_v = \begin{bmatrix} 0 \\ \hat{f}_v \end{bmatrix} \quad (5b)$$

The pseudo-time,  $\tau$ , bears no relation to the physical time,  $t$ . However at each physical time step the equation (4) may be iterated in pseudo-time. At convergence of the pseudo-time iterations (subiterations) the equations governing the unsteady flow are recovered. In the INS2D code the discretized equations are solved using a third-order upwind finite difference method and the solution is implicitly advanced using a Gauss-Seidel-type line relaxation.

### **2.3.2 Grid Generation**

The grids were generated using Gridgen.<sup>TM</sup> The grid points are clustered along the surface of the airfoil and at the leading and trailing edges to better resolve the flow features in these regions. The C-O grid has dimensions of 438×100. A typical grid is shown in Fig. 2.12. The far-field boundaries are placed 8 chord lengths from the airfoil.

A sequence of 36 grids each corresponding to the airfoil at 0.4° increments in the angle of attack 0.0°-14.4°-0.0° were generated. The INS2D code read in a new grid at each time-step so that the pitch-up and pitch-down motion of the airfoil could be simulated.

### **2.3.3 Boundary Conditions**

The boundary conditions are specified as follows. The airfoil surface is a moving, no-slip, wall boundary condition; the velocity matches the motion of the wall during pitch-up or pitch-down of the airfoil. The pressure is obtained by specifying zero wall-normal, pressure gradient. The farfield outer boundary is computed using a characteristic relation for the pressure. The velocities are based on the freestream velocity at the angle of attack that is superimposed on the velocities from a point vortex; this vortex is centered on the airfoil's quarter chord. At the downstream outflow boundary a constant

static pressure is used and the velocities are extrapolated from the interior. Along the wake-cut line of the C-grid the pressure and velocities are obtained from an average of the surrounding values.

The Gurney flap is modeled by blanking out the grid points “inside” the flap. The surface of the flap is treated as a moving, no-slip wall.

## **Chapter 3**

### **Results and Discussion**

The results of the experimental study of the effects of the Gurney flap on the stationary (3.1) and oscillating (3.2) airfoil flows are first presented. Then the computational predictions of the oscillating airfoil with Gurney flap (3.3) are discussed.

#### **3.1 Stationary Airfoil**

##### **3.1.1 Effect of Gurney Flap**

The phase reversals across the stagnation and laminar separation points are first examined for the stationary airfoil with no Gurney flap and 1.5% $c$  and 2.5% $c$  Gurney flaps at the maximum angle of attack of  $14.4^\circ$  and Reynolds number of 169,000. The phase reversal phenomenon was first observed by Stack et al<sup>43</sup> in their study of laminar separation on a low Reynolds number airfoil. Figure 3.1 shows example plots of the low-pass filtered data for sensors 11, 13, 15, 17 and 19 for the no Gurney flap case. An examination of these signals shows that there is a phase reversal between sensor pairs 13-15, 15-17 and 17-19. The phase angles measured from all adjacent pairs of hot-film sensors are shown in Figure 3.2. The phase angle is  $0^\circ$  across the sensor pairs 1-3 to 11-13, Fig. 3.2(a),  $180^\circ$  across the sensor pairs 13-15, 15-17 and 17-19 and again  $0^\circ$  across the sensor pair 19-21 to 29-31. The phase reversal across the sensor pair 13-15 is thought to indicate the leading edge separation point, which is thus located between  $s/c=0.033$  (on the lower surface of the airfoil) and  $s/c=0.0$ . The phase reversal between pairs 15-17 and 17-19 may indicate the separation and/or reattachment locations associated with a vortex

in the reversed flow region. These phase reversals are not so sharply defined but this may be due to the freestream turbulence levels in the NC State wind tunnel. McGhee et al<sup>52</sup> have noted that the turbulence levels have a strong influence on the characteristics of the laminar separation bubble on an airfoil.

The phase reversals for the 1.5%*c* Gurney flap case are examined in Figures 3.3 and 3.4. The time history plots for sensors 11-19 are shown in Figure 3.3. These show a phase reversal between the sensor pair 13-15 that is verified in the phase angle plots, Fig. 3.4. Unlike the no Gurney flap data shown in Figure 3.2, no phase reversal is observed across the sensor pairs 15-17 and 17-19. This may indicate that the leading edge separation and the vortex are now coinciding or that the vortex immediately downstream of the separation is eliminated. The low-pass filtered voltage signals for the 2.5%*c* Gurney flap case for sensors 11-19 are shown in Fig. 3.5. A phase reversal is seen across the sensor pair 13-15. The computed phase angle data for the 2.5%*c* Gurney flap case, Fig. 3.6, again verifies the phase reversal across the sensor pairs 13 and 15. A weak phase reversal is also observed across sensors 5 and 7, Fig. 3.6(a). This indicates the possible location of the stagnation point; however this feature was not detected for the no and 1.5%*c* Gurney flap cases.

In summary it appears that the effect of the Gurney flap is to either cause the flow phenomena occurring at the leading edge of the airfoil to merge together or eliminate the vortex. The location as the leading edge separation point appears to be unchanged.

### **3.1.2 Effect of Reynolds Number**

The phase reversals on the baseline airfoil are examined for the lower Reynolds number,  $Re=96,000$ , at  $\alpha= 14.4^\circ$ , Fig. 3.7 and 3.8. As with the time traces for the

Re=169,000 case presented in Fig. 3.1, the Re=96,000 case, Fig. 3.7, shows a phase reversal between sensors 13-15. This phase reversal is clearly observed for the sensor pair 13-15, Fig. 3.8(b), and indicates the leading edge separation. A possible phase reversal between sensors 15 and 17 is also evident. In addition the phase angle for the sensor pair 25-27, indicates a phase reversal that may be associated with the location of the vortex, Fig. 3.8(c). A comparison of the phase reversals for the lower and higher Reynolds numbers, Figs. 3.2 and 3.8, suggests that the location of the leading edge separation is unchanged, but that the vortex is moved forward with increasing Reynolds number.

The effect of Reynolds number on the airfoil with the 2.5%*c* Gurney flap is next examined. The oscillations in the time traces for Re=96,000, Fig.3.9, are not as pronounced as in the Re=169,000 case, Fig. 3.5. However the phase reversal across the sensor pair 13-15 is discernible. Figure 3.10(b) shows phase reversals between the sensor pair 13-15, which is an indicator of the leading edge separation location, and the sensor pair 15-17, that indicates the vortex. Thus increasing the Reynolds number appears to either eliminate the vortex or cause this vortex to move forward so that it is coincident with the separation point. In the following sections we examine the effect of Gurney flap height and Reynolds number on the unsteady boundary layer events as the airfoil is oscillated.

## **3.2 Oscillating Airfoil**

### **3.2.1 Oscillation to $\alpha_{\max}=7.2^\circ$**

The time histories of representative CVA outputs of the 2.5%*c* Gurney flap, Re=96,000 case for sensors 15 to 30 are shown in Figure 3.11. For sake of clarity the

data are equally offset for each successive sensor. At time  $t=0s$  the airfoil is at  $\alpha=0.0^\circ$ ; at time  $t=0.11s$  it has pitched up to  $7.2^\circ$ ; and then at time  $t=0.22s$ , it has been pitched back down to  $0.0^\circ$ . The loci of the three identifiable and characteristic inflexion points are also shown in the figure. These inflexion points are more clearly shown in Figure 3.12. Inflexion point 1 is associated with a local minimum in the time history. The standard deviation also increases across the minimum, and thus as described by Mangalam et al,<sup>53</sup> this inflexion point is associated with the onset of transition. The inflexion point 2 is associated with a local maximum in the time history, and denotes where the flow becomes fully turbulent. Finally the inflexion point 3 is also a local minimum in the time history, and is associated with the onset of laminar separation during pitch-down of the airfoil. Thus overall the following sequence of events are observed for the airfoil oscillated under “attached flow” conditions. During pitch-up, the transition location moves upstream. During pitch-down, the onset of separation of the laminar boundary layer moves downstream. The transition to fully turbulent flow also moves downstream and occurs, even further downstream than the separation. The effect of the Gurney flap and Reynolds number on these boundary layer events is discussed in greater detail below.

### **3.2.1.1 Effect of Gurney Flap**

The effect of the Gurney flap height on the boundary layer separation and transition is examined in Figures 3.13-3.15. During the pitch-up of the airfoil, there is no discernible effect on the transition at the lower Reynolds number,  $Re=96,000$ , Fig. 3.13. However during pitch-down there is a marked effect as the 2.5% $c$  Gurney flap advances both the laminar separation and transition to lower angles of attack. The 1.5% $c$  Gurney flap has the opposite effect as the 2.5% $c$  Gurney flap. At the moderate Reynolds number,

Fig. 3.14, it is seen that increasing the Gurney flap height advances the transition during pitch-up to lower angles of attack. The laminar separation during pitch-down is also advanced to lower angles of attack. There is no marked effect on the onset of turbulent flow, although the data suggest that these events may occur at a lower angle of attack during pitch-down. The effect of the Gurney flap at the largest Reynolds number,  $Re=192,000$ , is examined in Fig. 3.15. The unsteady transition location for the 1.5%*c* and 2.5%*c* Gurney flaps follow the same trends during pitch-up of the airfoil, where both are advanced to lower angles of attack. However during pitch-down the small Gurney flap behaves like the clean airfoil, while for the 2.5%*c* Gurney flap laminar separation occurs at lower angles of attack. During pitch-down, the transition with the 2.5%*c* Gurney flap is delayed, whereas the 1.5%*c* Gurney flap has no effect.

### **3.2.1.2 Effect of Reynolds Number**

The Reynolds number effects on the boundary layer separation and transition are examined in Figures 3.16–3.18. For the clean airfoil, Fig. 3.16 no Reynolds number effect is observed on the transition during pitch-up. However during pitch-down it is observed that the laminar separation is advanced to a higher angle of attack. As there is only a small effect on the transition location, it thus appears that the separation bubble is shorter with increasing Reynolds number. For the 1.5%*c* Gurney flap case, Fig. 3.17, increasing Reynolds number moves the transition to a lower angle of attack during the pitch-up of the airfoil. However during pitch-down, the location of separation is delayed at  $Re=169,000$  compared to  $Re=96,000$ , and is advanced at  $Re=192,000$  compared to  $Re=169,000$ . The location of transition shows a similar trend to the separation during pitch-down. A different Reynolds number effect is also observed for the largest Gurney

flap, Fig. 3.18. During pitch-up, the two higher Reynolds number are advanced to lower angles of attack compared to the  $Re=96,000$  cases with  $Re=169,000$  being the earliest. However, during pitch-down the two lower Reynolds numbers show the same behavior, whereas the  $Re=192,000$  case is delayed to a lower angle of attack. The 2.5%*c* Gurney flap appears to have no effect on the transition onset during pitch-down, although transition for the mid-range Reynolds number may occur at a slightly higher angle of attack.

### 3.2.2 Oscillation to $\alpha_{max}=14.4^\circ$

Representative time histories of the CVA outputs for sensors 15 to 30 are shown in Figure 3.19. These data are for the airfoil equipped with the 2.5%*c* Gurney flap, tested at  $Re=96,000$ . The voltage signals are again offset for clarity. At time  $t=0.0s$  the airfoil is at  $0.0^\circ$  angle of attack; at time  $t=0.11s$  the airfoil has pitched up to  $14.4^\circ$ ; and at time  $t=0.22s$  the airfoil is again at  $0.0^\circ$ . Also shown in this figure are the loci of the five inflexion points that are identified from an inspection of the individual CVA outputs. The inflexion point 1 is associated with a local minimum in the time history. For the sensors 15 to 21, the standard deviation in the time history is unchanged across this minimum, whereas for sensors 22 to 30 the standard deviation is increased following the minimum, Fig. 3.20. This increase in standard deviation indicates transition.<sup>53</sup> Thus in the range  $s/c \leq 0.133$  the inflexion point 1 indicates laminar separation and in the range  $s/c \geq 0.133$  the inflexion point indicates transition. The inflexion point 2 is associated with a local maximum in the time history. This maximum indicates the transition-to-turbulence of the separated shear layer. Thus it can be seen in Figure 3.19 that during the pitch-up of the airfoil, for  $t \leq 0.04s$ , the transition location in the attached boundary layer moves forward

rapidly. For  $t > 0.04s$  the laminar boundary layer separates, and the location of separation moves further forward with increasing  $\alpha$  (that is increasing time). The transition location of the separated shear layer moves aft as the angle of attack increases. The location of the turbulent reattachment of the shear layer is not captured, as there are no hot-film sensors downstream of  $s/c \approx 0.25$ .

The point of inflexion 3 is also associated with a local minimum in the time history, Fig. 3.20. No change in the standard deviation is observed across this minimum, and thus this inflexion point indicates a laminar separation during the pitch-down of the airfoil. The inflexion point 4 is associated with a local maximum in the time history, and thus indicates transition of the separated shear layer. The point of inflexion 5 is associated with a local minimum in the time history. This minimum is associated with the turbulent reattachment of the shear layer during pitch-down of the airfoil. It is evident that during the pitch-down the laminar separation bubble moves aft on the airfoil.

### **3.2.2.1 Effect of Gurney Flap**

The effect of the Gurney flap on the locations of laminar separation and transition-to-turbulence during pitch-up is shown in Figures 3.21–3.23. At  $Re=96,000$ , Fig. 3.21, the Gurney flap has little or no effect on the location of laminar separation. The effect of the Gurney flap on the transition location is small, and for both the attached boundary layer and the separated shear layer, transition occurs at slightly lower angles of attack. Thus although the turbulent reattachment location is not captured, at a given angle of attack it appears that the leading edge separation bubble is longer with a Gurney flap. At  $Re=169,000$ , Fig. 3.22, the Gurney flap has no marked effect on the loci associated with the point of inflexion 1. However as with the lower Reynolds number the transition

in the separated shear layer is moved aft with the Gurney flaps. At  $Re=192,000$ , Fig. 3.23, the effect of the Gurney flap is most clearly seen. The onset of transition and laminar separation are advanced to lower angles of attack; the largest Gurney flap, 2.5%c, is observed to be the most effective in this regard. Thus at a given angle of attack, the extent of the separated flow is larger with the Gurney flap, and is largest for the largest Gurney flap.

The effect of the Gurney flap on the unsteady separation, transition and reattachment locations during pitch-down is shown in Figures 3.24-3.26. For the low Reynolds number,  $Re=96,000$ , the clean airfoil and 2.5%c Gurney flap follow the same trend, Fig 3.24. However the 1.5%c Gurney flap advances all the boundary layer events to higher angles of attack. Thus during pitch-down, at a given angle of attack the extent of the separation bubble is greater for the 1.5%c Gurney flap compared to the other two cases. At  $Re=169,000$ , Fig. 3.25, the Gurney flap is observed to delay the onset of laminar separation, transition and turbulent reattachment to lower angles of attack. Although both Gurney flaps have the same effect on the transition and reattachment locations, the 2.5%c Gurney flap delays the laminar separation more than the 1.5%c Gurney flap. Thus it is apparent that the Gurney flap results in a larger leading edge separation bubble. At the largest Reynolds number,  $Re=192,000$ , Fig. 3.26, there is no clear effect when the 1.5%c Gurney flap is compared with the clean airfoil. However the 2.5%c Gurney flap delays separation and transition to lower angles of attack, but has no clear effect on the location of turbulent reattachment.

### **3.2.2.2 Effect of Reynolds Number**

The Reynolds number effect on the unsteady boundary layer events during pitch-up is examined for the clean airfoil and two Gurney flap heights in Figures 3.27-3.29. On the clean airfoil, Fig. 3.27, increasing the Reynolds number advances the laminar separation and transition to lower angles of attack. It is interesting to note that effect is more marked for the intermediate Reynolds number,  $Re=169,000$ , compared to the  $Re=192,000$  case. Thus during pitch-up, at a given angle of attack laminar separation occurs further forward, and the transition occurs at a more downstream location. For the 1.5% $c$  Gurney flap, Fig. 3.28, the Reynolds number effect is monotonic – that is increasing the Reynolds number progressively advances the separation and transition locations to lower angles of attack. This Reynolds number effect is more marked for the 2.5% $c$  Gurney flap case, Fig. 3.29. For both Gurney flap cases it is evident that the leading edge separation bubble is more elongated with increasing Reynolds number.

The effects of Reynolds number on the unsteady separation, transition and reattachment locations during pitch-down are examined in Figures 3.30–3.32. For the clean airfoil, Fig. 3.30, the increasing Reynolds number advances all locations to higher angles of attack. Therefore at a given angle of attack a longer separation bubble results. However the  $Re=169,000$  case results in a larger bubble than the  $Re=192,000$  case. The effect of Reynolds number on the 1.5% $c$  Gurney flap case is shown in Fig. 3.31. Increasing the Reynolds number advances the laminar separation to higher angles of attack. However the location of turbulent reattachment is delayed to lower angles of attack for the initial pitch-down motion for the  $Re=169,000$  case; over the latter portion of the pitch-down the turbulent reattachment is advanced. For the  $Re=192,000$  case the turbulent reattachment is advanced to higher angles of attack over the range of

measurements. There is little difference in the transition locations of  $Re=96,000$  and  $169,000$  cases; however the transition is advanced to a higher angle of attack for the  $192,000$  case. For the  $2.5\%c$  Gurney flap, Fig. 3.32, the two higher Reynolds number cases follow similar trends. The laminar separation and transition locations are advanced to a higher angles of attack compared to the  $Re=96,000$  case. The turbulent reattachment is advanced to higher angles of attack for  $Re=192,000$  compared to  $Re=96,000$ . However during the initial pitch-down the  $Re=96,000$  and  $Re=169,000$  cases follow the same trend, while in the later stages of the pitch-down the two higher Reynolds numbers ( $Re=169,000$  and  $192,000$ ) show the same effect.

### **3.3 Flowfield Computations**

The experimental observations of the effect of the Gurney flap on the unsteady airfoil flow were verified by predictions from Navier-Stokes simulations. The case examined is the light dynamic stall ( $\alpha=0.0^\circ-14.4^\circ$ ) with a clean airfoil and  $2.5\%c$  Gurney flap, at a Reynolds number of  $169,000$ . In the results presented below the instantaneous streamlines, surface and flowfield pressures, streamwise velocity and skin-friction are examined at intervals of  $2.4^\circ$  during pitch-up and pitch-down of the airfoil.

#### **3.3.1 Streamlines and Pressure Contours**

##### **3.3.1.1 No Gurney Flap**

The instantaneous streamlines superimposed on the flowfield pressure contours during pitch-up of the airfoil are shown in Figure 3.33. The leading edge separation bubble is first observed at  $\alpha=2.4^\circ$ . The separation point is located at  $s/c\approx 0.16$  and the reattachment is located at  $s/c\approx 0.24$ , which are in good agreement with the experimental results, Fig. 3.22. At  $\alpha=9.6^\circ$  the bubble is more elongated; the location of separation is

moved forward and the reattachment is moved aft. The separation at  $\alpha=12.0^\circ$  is located even further forward, at  $s/c\approx 0.02$ , and the reattachment location is further downstream. At the maximum angle of attack,  $\alpha=14.4^\circ$ , the separation bubble has detached from the airfoil's surface, to form the expected leading edge dynamic stall vortex. This vortex has a clockwise rotation and convected downstream to  $s/c\approx 0.46$ .

During pitch-down, at  $\alpha=12^\circ$ , three vortical structures form on the upper surface of the airfoil, Fig. 3.34. The dynamic stall vortex is furthest downstream at  $s/c\approx 0.67$ . A second vortex, also with a clockwise rotation, is centered at  $s/c\approx 0.28$ ; the vortex is shed from the leading edge. A third, counter-clockwise rotating vortex, is formed between these two vortices and is located near mid-chord of the airfoil. The three vortices are convected downstream as the airfoil pitches down as seen at  $\alpha=9.6^\circ$ . At  $\alpha=9.6^\circ$  the counter-clockwise rotating vortex is detached from the surface and the flow along the airfoil surface is attached to the surface over the range  $0.56 \leq s/c \leq 1.0$ . The reattachment location moves downstream along the airfoil as the pitch-down of the airfoil is continued. At  $\alpha=7.2^\circ$  and  $4.8^\circ$  the flow separation is limited to a small region near the trailing edge. The flow is fully attached by  $\alpha=2.4^\circ$ .

### **3.3.1.2 Gurney Flaps**

The sequence of instantaneous streamlines and pressure contours for the airfoil with 2.5%*c* Gurney flap is shown in Figures 3.35 and 3.36. During pitch-up of the airfoil, Fig. 3.35, the sequence differs very little from the no Gurney flap case, Fig. 3.33. This verifies the observation in the experiment, Fig. 3.22, that there is little effect of the Gurney flap during pitch-up. However during pitch-down, Fig 3.36 compared with Fig.

3.34, several differences are observed. At  $\alpha=12.0^\circ$ , there is a larger region of high pressure on the airfoil's lower surface for the 2.5%*c* Gurney flap case. At  $\alpha=9.6^\circ$ , whereas the no Gurney flap case shows the single dynamic stall vortex at the airfoil's trailing edge, with the Gurney flap a pair of vortices are observed. The second vortex is thought to arise from the vortices that are alternately shed from the Gurney flap. At  $\alpha=7.2^\circ$ , the trailing edge vortex is more pronounced with the Gurney flap. At the lower angles of attack the increased turning of the flow at the airfoil's trailing edge is the most pronounced feature in the flowfield.

In summary, as the airfoil pitches downwards the effect of the Gurney flap is to decrease the pressure on the upper surface of the airfoil and increase the pressure on the lower surface, compared with the clean airfoil case. The addition of the Gurney flap generates a region of higher pressure to form on the lower surface at the trailing edge which would lead to an increase in the nose-down pitching moment. This is an expected result found in previous research in steady flows.<sup>1,3,4</sup> An examination of the locus of the separation location shows that the effect of the Gurney flap is to move the separation forward on the airfoil at each angle of attack. This observation is consistent with the experiments, Fig. 3.25. Figures 3.41 and 3.42 show comparisons of the flow phenomena loci found in the computations versus the experimental work. These figures show that the computations verify the experimental work.

### **3.3.2 Velocity Contours**

#### **3.3.2.1 No Gurney Flap**

The contours of the instantaneous velocity are presented in Figure 3.39 for the airfoil during pitch-up. The green color contours show regions of low magnitude

velocities and may be identified with the boundary layer and wake. As the airfoil's angle of attack is increased the boundary layer on the upper surface, and the airfoil's wake thickens. At  $\alpha=9.6^\circ$ , reversed flow (as denoted by blue colored contours) is first observed near the airfoil's leading edge. The extent of this reversed flow region increases with the increasing angle of attack.

The instantaneous velocity contours during pitch-down are shown in Figure 3.40. At  $\alpha=12.0^\circ$  the reversed flow regions that are associated with the clockwise vortices and the attached flow region associated with the counter-clockwise vortex can be seen. The high velocity region that is shed off the airfoil with the stall vortex can be seen at  $\alpha=9.6^\circ$ . The low velocity flow in the vicinity of the stagnation point diminishes in size during the pitch-down. The airfoil wake airfoil extends upwards during the pitch-down through  $\alpha=0.0^\circ$ .

### **3.3.2.2 Gurney Flaps**

Velocity contours during pitch-up for the airfoil with the 2.5%*c* Gurney flap, Fig. 3.41, are similar to those previously observed for the clean airfoil case, Fig. 3.39. During pitch-down three primary effects are observed. First, the Gurney flap causes regions of higher velocity to form outside of the boundary layer on the upper surface of the airfoil, Fig. 3.42. This is due to the increased airfoil circulation that is generated by the Gurney flap. The second effect of the Gurney flap is to pull the wake downward during pitch-down. This is seen from the downward shift in the green color contour when Figures 3.40 and 3.42 are compared. Finally, the stagnation point is also shifted further towards the lower airfoil surface during pitch-down due to the Gurney flap as can be seen by again comparing Figures 3.40 and 3.42.

### 3.3.3 Surface Pressure Coefficient

#### 3.3.3.1 No Gurney Flap

The instantaneous surface pressure coefficients are shown in Figure 3.43. These show the evolution of the dynamic stall vortex and other boundary layer events that have been described above. During the pitch-up of the airfoil the distribution of pressure on the airfoil's lower surface changed very little, but the pressure become increasingly positive as the angle of attack is increased. The stagnation point can be identified from the location where  $C_p=1$ , and is seen to move rearward as the angle of attack is increased. During pitch-down the stagnation points move back towards the airfoil's leading edge.

On the upper surface of the airfoil as the angle of attack is increased during pitch-up, an increasingly large region of negative pressure coefficients is seen. At the lower angles of attack  $\alpha \leq 12.0^\circ$ , this region is associated with the increasingly large region of reversed flow. However at  $\alpha = 14.4^\circ$ , the dynamic stall vortex has formed, and its presence is clearly marked by the distinctive suction peak at  $x/c \approx 0.5$ . During pitch-down of the airfoil, at  $\alpha = 12.0^\circ$  the suction peak is located at  $x/c \approx 0.68$ . The rapid passage of the dynamic stall, is noted by the trailing edge suction pressure seen at  $\alpha = 9.6^\circ$ . The subsequent loss of lift due to the shedding of the dynamic vortex is evident for  $\alpha < 9.6^\circ$  as the magnitudes of the pressure coefficients are very small.

#### 3.3.3.2 Gurney Flaps

The instantaneous surface pressure coefficients are shown in Figure 3.44. The instantaneous pressures for the 2.5% c Gurney flap differ little from the no Gurney flap case. However at the trailing edge of the airfoil there is a larger pressure difference between the upper and lower surface of the airfoil. During the pitch-down of the airfoil

there are more substantive differences. At  $\alpha=12.0^\circ$  the no Gurney and 2.5%c Gurney flap case are quite similar. At  $\alpha=9.6^\circ$  the multiple vortex structure observed in the plot of the streamlines results in a significant extent of negative pressure coefficient over the aft portion of the airfoil. This is in contrast to the no Gurney flap case, which shows only negative pressure coefficients at the airfoil's trailing edge. The negative pressure coefficients are still observed at  $\alpha=7.2^\circ$  for the 2.5%c Gurney flap, where as for the no Gurney flap the magnitude of the pressure coefficients is very small.

### **3.3.4 Skin Friction Coefficient**

#### **3.3.4.1 No Gurney Flap**

The instantaneous skin-friction coefficients are shown in Figure 3.45. During the pitch-up and pitch-down of the airfoil the skin-friction along the lower surface is largely positive indicating the flow along this surface remains attached. On the airfoil's upper surface there are regions of increasingly large reversed flow as the airfoil is pitched-up, and these are denoted by the negative skin-friction. At  $\alpha=14.4^\circ$  the negative skin-friction is most pronounced beneath the dynamic stall vortex. As the airfoil is pitched down the extent of reversed flow is reduced, and for  $\alpha<7.2^\circ$  the flow is wholly attached. It is also interesting to note that there are variations in the skin-friction over the aft portion of the airfoil for  $\alpha=9.6^\circ$  and  $12.0^\circ$ ; these variations are associated with the vortical structure that was previously discussed.

#### **3.3.4.2 Gurney Flaps**

The sequence of instantaneous skin-friction distributions for the airfoil with Gurney is shown in Figure 3.46. The variation in skin-friction during pitch-up shows little difference compared to the no Gurney flap case. This is consistent with our

previous observations that show little change during pitch-up. During pitch-down of the airfoil, the overall skin-friction distribution is also similar to the no Gurney flap case. However in the leading edge region, near the start of the pitch-down,  $\alpha=9.6^\circ$  and  $12.0^\circ$ , there is little movement of the separation location with the Gurney flap. This is in contrast to the Gurney flap case, which shows a marked movement of the leading edge separation.

### **3.3.5 Lift and Drag**

The variations in the lift and drag during the pitch-up and pitch-down of the airfoil are shown in Figure 3.47. During pitch-up of the airfoil the slope of the lift curve is constant. Overall the slope is unchanged with the addition of the Gurney flap except at the low angles of attack where the Gurney flap slightly increases lift. During pitch-down the 2.5%*c* Gurney flap causes an increase in lift compared to the no Gurney flap case from  $\alpha=13.5^\circ$  until the airfoil has reached  $\alpha=0.0^\circ$ . The increment in the lift is in the range 0.2-0.5 during pitch-down. The lift is increased by  $\Delta C_l = 0.56$  at the end of pitch-down. This result shows that the effect of the dynamic stall vortex is potentially less catastrophic with the Gurney flap. However, the shedding of the vortices still causes oscillations in the lift during pitch-down.

The time history of the drag coefficient shows that while the drag is unchanged during pitch-up of the airfoil, the drag increases during the pitch-down. Thus as with the stationary airfoil the increase in lift with the use of the Gurney flap comes with a drag penalty.

# Chapter 4

## Concluding Remarks

### 4.1 Summary of Results

The effect of a Gurney flap on the unsteady flow past an airfoil is experimentally and computationally examined. Experiments have been performed on a *NACA0012* airfoil with and without Gurney flaps for both stationary and oscillating conditions. The Reynolds numbers based on airfoil chord are 96,000, 169,000 and 192,000, and the Gurney flap heights are 1.5% and 2.5% of the chord. The angles of attack examined, for the stationary airfoil, are  $7.2^\circ$  and  $14.4^\circ$ . For the oscillating airfoil two conditions were examined: attached flow where the airfoil was oscillated between  $0.0^\circ$  and  $7.2^\circ$  at a pitch rate of  $65.45^\circ/sec$ ; and light dynamic stall, with oscillations between  $0.0^\circ$  and  $14.4^\circ$  at a pitch rate of  $130.9^\circ/sec$ . The frequency of the oscillations is  $4.5Hz$ .

The airfoil was instrumented with an array of multiple, surface mounted hot-film sensors that are operated with a multi-channel constant voltage anemometer system. Phase reversals were examined for the stationary airfoil to determine the location of the stagnation, separation and possible reattachment locations. In the cases of the oscillating airfoil, the characteristics of the inflexion points in the time histories of the anemometer output are examined to determine the locations of laminar boundary layer separation, transition-to-turbulence, and turbulent reattachment.

For the stationary airfoil at  $\alpha=14.4^\circ$ , the Gurney flap is observed to move the secondary vortex forward on the airfoil so that it either coincides with the separation location or eliminates this vortex altogether. In the case of the oscillating airfoil the

Gurney flap the laminar separation and onset of transition are moved forward on the airfoil.

Increasing the Reynolds number for the stationary airfoil without the Gurney flap causes the secondary vortex to move forward on the airfoil. The same effect is observed when the Reynolds number is increased for the 2.5%*c* Gurney flap case. In the cases of the oscillating airfoil, during pitch-up the leading-edge separation bubble is more elongated and during pitch-down the bubble is moved aft on the airfoil.

Incompressible RANS computations were performed for the airfoil in light dynamic stall conditions at  $Re=169,000$  with and without the 2.5%*c* Gurney flap. The computations support the findings of the experimental work and provide insight as to the effect of the Gurney flap on the aerodynamic loads and moments. From the computations it is observed that the Gurney flap increases the amount of lift generated by the airfoil during pitch-down by as much as  $\Delta C_l$  of 0.56 during the pitch-down. However this increase in lift was accompanied with an increase in drag.

#### **4.2 Recommendations for Future Work**

It is recommended for future work that the airfoil be equipped with additional hot-film sensors along the entire upper and lower surfaces. An improved spatial resolution of the hot-film sensors is also desirable. Thus a more complete documentation of the flow phenomena on the airfoil can be obtained. In addition the airfoil should be equipped with surface pressure taps to determine the aerodynamic loads and moments. These loads and moments should then be correlated with the hot-film sensor measurements and the results of Navier-Stokes computations.

## Chapter 5

### References

1. Liebeck, R. H., "Design of Subsonic Airfoils for High Lift," *Journal of Aircraft*, Vol. 15, September 1978, pp. 547-561.
2. Henne, P. A., "Innovation with Computational Aerodynamics: The Divergent Trailing Edge Airfoil," *Progress in Astronautics and Aeronautics*, Vol. 125, AIAA Washington, 1990.
3. Giguère, P., Lemay, J. and Dumas, G., "Gurney Flap Effects and Scaling for Low-Speed Airfoils," *AIAA Paper 95-1881*, June 1995.
4. Myose, R., Papadakis, M. and Heron, I., "Gurney Flap Experiments on Airfoils, Wings, and Reflection Plane Model," *Journal of Aircraft*, Vol. 35, March-April 1998, pp. 206-211.
5. Neuhart, D. H. and Pendergraft, O. C., Jr., "A Water Tunnel Study of Gurney Flaps," *NASA TM 4071*, November 1988.
6. Jeffrey, D., Zhang, X. and Hurst, D. W., "Aerodynamics of Gurney Flaps on a Single-Element High-Lift Wing," *Journal of Aircraft*, Vol. 37, March-April 2000, pp. 295-301.
7. Bloy, A. W. and Durant, M. T., "Aerodynamic Characteristics of an Aerofoil with Small Trailing Edge Flaps," *Wind Engineering*, Vol. 19, No. 3, 1995, pp. 167-172.
8. Storms, B. L. and Jang, C. S., "Lift Enhancement of an Airfoil using a Gurney Flap and Vortex Generators," *Journal of Aircraft*, Vol. 31, March 1994, pp. 542-547.
9. Jang, C. S., Ross, J. C. and Cummings, R. M., "Computational Evaluation of an Airfoil with a Gurney Flap," *AIAA Paper 92-2708*, June 1992.
10. Ross, J. C., Storms, B. L. and Carrannanto, P. G., "Lift-Enhancing Tabs on Multielement Airfoils," *Journal of Aircraft*, Vol. 32, May-June 1995, pp. 649-655.
11. Carrannanto, P. G., Storms, B. L., Ross, J. C. and Cummings, R. M., "Navier-Stokes Analysis of Lift-Enhancing Tabs on Multi-Element Airfoils," *Aircraft Design*, Vol. 1, 1998, pp. 145-158.
12. Janus, M., "Analysis of Industrial Fan Designs with Gurney Flaps," *AIAA Paper 2000-0983*, January 2000.

13. McCroskey, W. J., "Unsteady Airfoils," *Annual Review of Fluid Mechanics*, Vol. 14, 1982, pp. 285-311.
14. Carr, L. W., "Progress in Analysis and Prediction of Dynamic Stall," *Journal of Aircraft*, Vol. 25, January 1988, pp. 6-17.
15. Carr, L. W. and McCroskey, W. J., "A Review of Recent Advances in Computational and Experimental Analysis of Dynamic Stall," *Proceedings of IUTAM Symposium on Fluid Dynamics of High Angle of Attack*, Tokyo, Japan, September 1992, pp. 3-31.
16. Carr, L. W. and Chandrasekhara, M. S., "Compressibility Effects on Dynamic Stall," *Progress in Aerospace Sciences*, Vol. 32, 1996, pp. 523-573.
17. Carr, L. W., McAlister, K. W. and McCroskey, W. J., "Analysis of the Development of Dynamic Stall based on Oscillating Airfoil Experiments," *NASA TN D-8382*, January 1977.
18. Lorber, P. and Carta, F., "Unsteady Transition Measurements on a Pitching Three-Dimensional Wing," *5<sup>th</sup> Symposium on Numerical and Physical Aspects of Aerodynamic Flows*, January 1992.
19. Schreck, S. J., Faller, W. E. and Robinson, M. C., "Unsteady Separation Processes and Leading Edge Vortex Precursors: Pitch Rate and Reynolds Number Influences," *AIAA Paper 2000-2605*, June 2000.
20. Lee, T. and Basu, S., "Measurement of Unsteady Boundary Layer Developed on an Oscillating Airfoil using Multiple Hot-Film Sensors," *Experiments in Fluids*, Vol. 25, 1998, pp. 108-117.
21. Carr, L. W., Chandrasekhara, M. S., Ahmed, S. and Brock, N. J., "Study of Dynamic Stall Using Real-Time Interferometry," *Journal of Aircraft*, Vol. 31, April 1993, pp. 991-994.
22. Ahmed, S. and Chandrasekhara, M. S., "Reattachment Studies of an Oscillating Airfoil Dynamic Stall Flowfield," *AIAA Journal*, Vol. 32, May 1994, pp. 1006-1012.
23. Chandrasekhara, M. S., Wilder, M. C. and Carr, L. W., "Competing Mechanisms of Compressible Dynamic Stall," *AIAA Journal*, Vol. 36, March 1998, pp. 387-393.
24. Aso, S. and Hayashi, M., "Experimental and Computational Studies on Dynamic Stall in Low Speed Flows," *Proceedings of IUTAM Symposium on Fluid Dynamics of High Angle of Attack*, Tokyo, Japan, September 1992, pp. 67-78.
25. Ko, S. and McCroskey, W. J., "Computations of Unsteady Separating Flows over an Oscillating Airfoil," *AIAA Paper 95-0312*, January 1995.

26. Badcock, K. J., Cantariti, F., Hawkins, I., Woodgate, M., Dubuc, L. and Richards, B. E., "Simulation of Unsteady Turbulent Flows around Moving Aerofoils using the Pseudo-Time Method," *International Journal for Numerical Methods in Fluids*, Vol. 32, No. 5, 2000, pp. 585-604.
27. Karim, M. A. and Acharya, M., "Suppression of Dynamic-Stall Vortices over Pitching Airfoils by Leading-Edge Suction," *AIAA Journal*, Vol. 32, August 1994, pp. 1647-1655.
28. Alrefai, M. and Acharya, M., "Controlled Leading-Edge Suction for Management of Unsteady Separation over Pitching Airfoils," *AIAA Journal*, Vol. 34, November 1996, pp. 2327-2336.
29. Weaver, D., McAlister, K. W. and Tso, J., "Suppression of Dynamic Stall by Steady and Pulsed Upper-Surface Blowing," *AIAA Paper 98-2413*, June 1998.
30. Greenblatt, D. and Wygnanski, I., "Dynamic Stall Control by Periodic Excitation, Part I: NACA 0015 Parametric Study," *Journal of Aircraft*, Vol. 38, May-June 2001, pp. 420-438.
31. Greenblatt, D., Neuburger, D. and Wygnanski, I., "Dynamic Stall Control by Intermittent Periodic Excitation," *Journal of Aircraft*, Vol. 38, May-June 2001, pp. 188-190.
32. Yu, Y. H., Lee, S., McAlister, K. W., Tung, C. and Wang, C. M., "Dynamic Stall Control for Advanced Rotorcraft Application," *AIAA Journal*, Vol. 33, February 1995, pp. 289-295.
33. Carr, L. W., Chandrasekhara, M. S., Wilder, M. C. and Noonan, K. W., "The Effect of Compressibility on Suppression of Dynamic Stall using a Slotted Airfoil," *AIAA Paper 98-0332*, January 1998.
34. Chandrasekhara, M. S., Wilder, M. C. and Carr, L. W., "Unsteady Stall Control using Dynamically Deforming Airfoils," *AIAA Journal*, Vol. 36, October 1998, pp. 1792-1800.
35. Hanratty, T. J. and Campbell, J. A., "Measurement of Wall Shear Stress," in *Fluid Mechanics Measurement*, edited by R. S. Goldstein, Taylor and Francis, Washington DC, 1996, Chapter 9.
36. Fage, A. and Falkner, V. M., "On the Relation between Heat Transfer and Surface Friction for Laminar Flow," *Aeronautical Research Council R. & M. No. 1408*, April 1931.

37. Ludwig, H., "Instrument for Measuring the Wall Shearing Stress of Turbulent Boundary Layers," *NACA TM 1284*, May 1950.
38. Liepmann, H. W. and Skinner, G. T., "Shearing-Stress Measurements by Use of a Heated Element," *NACA TN 3268*, November 1954.
39. Bellhouse, B. J. and Schultz, D. L., "Determination of Mean and Dynamic Skin-Friction, Separation and Transition in Low-Speed Flow with a Thin-Film Heated Element," *Journal of Fluid Mechanics*, Vol. 24, 1966, part 2, pp. 379-400.
40. Menendez, A. N. and Ramaprian, B. L., "The Use of Flush-Mounted Hot-Film Gauges to Measure Skin Friction in Unsteady Boundary Layers," *Journal of Fluid Mechanics*, Vol. 161, 1985, pp. 139-159.
41. Cook, W. J., "Response of Hot-Element Wall Shear Stress Gages in Unsteady Turbulent Flows," *AIAA Journal*, Vol. 32, July 1994, pp. 1464-1473.
42. Stack, J. P., Mangalam, S. M. and Berry, S. A., "A Unique Measurement Technique to Study Laminar-Separation Bubble Characteristics on an Airfoil," *AIAA Paper 87-1271*, June 1987.
43. Stack, J. P., Mangalam, S. M. and Kalburgi, V., "The Phase Reversal Phenomenon at Flow Separation and Reattachment," *AIAA Paper 88-0408*, January 1988.
44. Moes, T. R., Sarma, G. R. and Mangalam, S. M., "Flight Demonstration of a Shock Location Sensor Using Constant Voltage Hot-Film Anemometry," *NASA TM 4806*, August 1997.
45. Comte-Bellot, G., "Hot-Wire Anemometry," in *Handbook of Fluid Dynamics*, edited by R. W. Johnson, CRC Press, Boca Raton FL, 1998, Chapter 34.
46. Sarma, G. R., "Flow Measuring Apparatus," *US Patent 5074147*, December 1991.
47. Sarma, G. R., "Analysis of a Constant Voltage Anemometer Circuit," *Proceedings of IEEE Instrumentation and Measurement Technology Conference*, Irvine CA, May 1993, pp. 731-736.
48. Sarma, G. R., "Transfer Function Analysis of the Constant Voltage Anemometer," *Review of Scientific Instruments*, Vol. 69, June 1998, pp. 2385-2391.
49. Drela, M., "XFOIL: An Analysis and Design System for Low Reynolds Number Airfoils," *Low Reynolds Number Aerodynamics*, edited by T. J. Mueller, Vol. 54 *Lecture Notes in Engineering*, Springer-Verlag, New York, June 1989, pp. 1-12.

50. Kaiser, J. F. and Reed, W. A., "Data Smoothing using Low-Pass Digital Filters," *Review of Scientific Instruments*, Vol. 48, November 1977, pp. 1447-1457.
51. Rogers, S. E. and Kwak, D., "An Upwind Differencing Scheme for the Time-Accurate Incompressible Navier-Stokes Equations," *AIAA Journal*, Vol. 28, February 1990, pp. 253-262.
52. McGhee, R. J., Jones, G. S. and Jouty, R., "Performance Characteristics from Wind-Tunnel Tests of a Low-Reynolds-Number Airfoil," *AIAA Paper 88-0607*, January 1988.
53. Mangalam, S. M., Stack, J. P. and Sewall, W. G., "Simultaneous Detection of Separation and Transition in Surface Shear Layers," *Fluid Dynamics of Three-Dimensional Turbulent Shear Flows and Transition*, AGARD CP-438, Paper 12, October 1989.

# Chapter 6

## Tables

**Table 2.1: Sensor locations and resistances.**

<b>Sensor No.</b>	<b>Bank – Sensor No.</b>	<b>s/c</b>	<b>Sensor Resistance (W)</b>
1	1-1	0.2333	7.3
2	1-2	0.2167	7.3
3	1-3	0.2	7.2
4	1-4	0.1833	7.1
5	2-1	0.1667	7.2
6	2-2	0.15	7.1
7	2-3	0.133	7.2
8	2-4	0.1167	7.2
9	3-1	0.1	7.1
10	3-2	0.0833	7.2
11	3-3	0.0667	7.2
12	3-4	0.05	7.3
13	4-1	0.0333	7.4
14	4-2	0.0167	7.3
15	4-3	0.0	7.3
16	4-4	0.0167	7.2
17	5-1	0.0333	7.3
18	5-2	0.05	7.4
19	5-3	0.0667	7.2
20	5-4	0.0833	7.3
21	6-1	0.1	7.7
22	6-2	0.1167	7.3
23	6-3	0.1333	7.2
24	6-4	0.15	7.1
25	7-1	0.1667	7.2
26	7-2	0.1833	7.1
27	7-3	0.2	7.3
28	7-4	0.2167	7.3
29	8-1	0.2333	7.2
30	8-2	0.25	7.3
31	8-3	0.2667	7.2
32	8-4	0.2833	7.2

**Table 3.1: Stagnation, separation, reattachment and vortex core locations (in terms of s/c) during pitch-up for airfoil with no Gurney flap and Re=169,000.**

a	Stagnation Point	Separation	Reattachment	Stall Vortex Core
2.4°	0.006	0.17	0.24	0.20
4.8°	0.012	0.065	0.31	0.23
7.2°	0.021	0.052	0.20	0.1
9.6°	0.029	0.040	0.29	0.15
12.0°	0.039	0.025	0.49	0.29
14.4°	0.048	0.0	0.65	0.50

**Table 3.2: Stagnation, separation and reattachment locations (in terms of s/c) during pitch-down for airfoil with no Gurney flap and Re=169,000.**

a	Stagnation Point	Separation	Reattachment
12.0°	0.038	0.0	n/a
9.6°	0.025	0.061	n/a
7.2°	0.019	0.82	n/a
4.8°	0.015	0.82	n/a
2.4°	0.010	n/a	n/a
0.0°	0.002	n/a	n/a

**Table 3.3: Vortex separation and reattachment locations (in terms of s/c) during pitch-down for airfoil with no Gurney flap and Re=169,000.**

a	Vortex 1		Vortex 2		Vortex 3	
	Separation	Reattachment	Separation	Reattachment	Separation	Reattachment
12.0°	0.0	0.34	0.56	0.34	0.56	1.0
9.6°	0.06	0.56	n/a	n/a	n/a	n/a
7.2°	0.82	1.0	n/a	n/a	n/a	n/a

**Table 3.4: Vortex core locations (in terms of s/c) during pitch-down for airfoil with no Gurney flap and Re=169,000.**

a	Vortex 1 Core	Vortex 2 Core	Vortex 3 Core
12.0°	0.28	0.43	0.67
9.6°	0.5	0.71	1.0
7.2°	1.0	n/a	n/a

**Table 3.5: Stagnation, separation, reattachment and vortex core locations (in terms of s/c) during pitch-up for airfoil with 2.5%*c* Gurney flap and Re=169,000.**

a	Stagnation Point	Separation	Reattachment	Stall Vortex Core
2.4°	0.007	0.16	0.24	0.2
4.8°	0.01	0.054	0.27	0.15
7.2°	0.02	0.03	0.3	0.11
9.6°	0.03	0.03	0.51	0.13
12.0°	0.04	0.02	0.48	0.3
14.4°	0.05	0.01	0.67	0.49

**Table 3.6: Stagnation, separation and reattachment locations (in terms of s/c) during pitch-down for airfoil with 2.5%*c* Gurney flap and Re=169,000.**

a	Stagnation Point	Separation	Reattachment
12.0°	0.037	0.026	n/a
9.6°	0.028	0.045	0.59
7.2°	0.024	0.25	n/a
4.8°	0.019	0.57	n/a
2.4°	0.014	0.77	n/a
0.0°	0.009	n/a	n/a

**Table 3.7: Vortex separation and reattachment locations (in terms of s/c) during pitch-down for airfoil with 2.5%*c* Gurney flap and Re=169,000.**

a	Vortex 1		Vortex 2		Vortex 3	
	Separation	Reattachment	Separation	Reattachment	Separation	Reattachment
12.0°	0.026	0.35	0.35	0.58	0.58	n/a
9.6°	0.045	0.59	n/a	n/a	n/a	n/a
7.2°	0.8	n/a	n/a	n/a	n/a	n/a

**Table 3.8: Vortex core locations (in terms of s/c) during pitch-down for airfoil with 2.5%*c* Gurney flap and Re=169,000.**

a	Vortex 1 Core	Vortex 2 Core	Vortex 3 Core
12.0°	0.28	0.44	0.69
9.6°	0.52	0.75	1.1
7.2°	0.89	n/a	n/a

# Chapter 7

## Figures

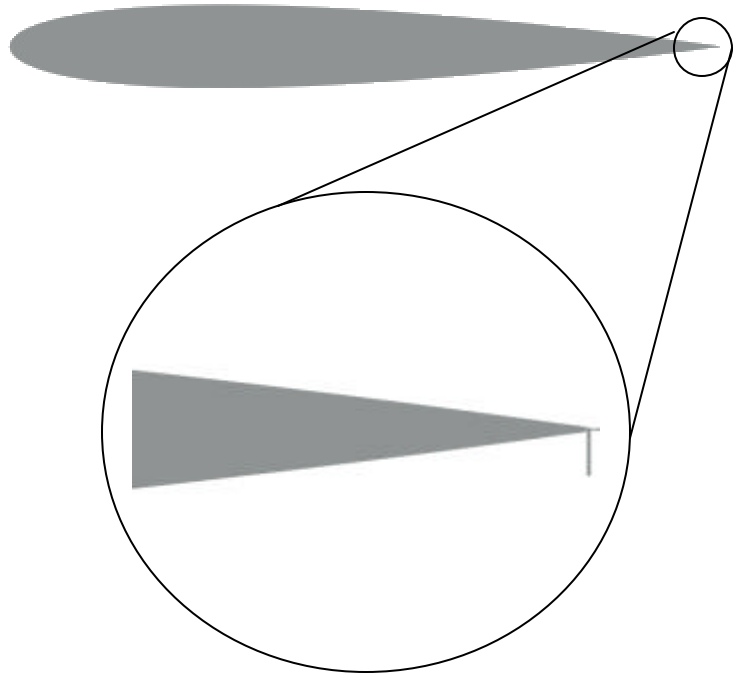


**Figure 1.1: Illustration of a 2.5%*c* Gurney flap.**

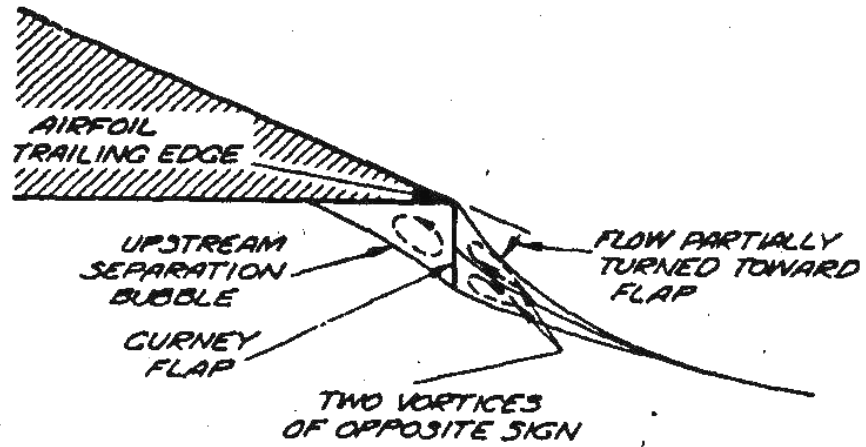
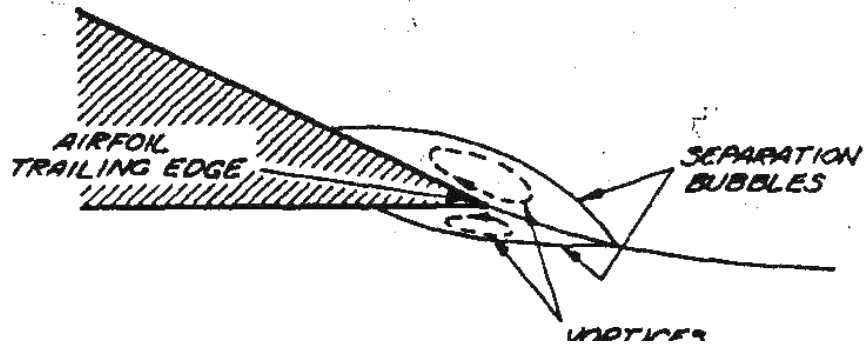
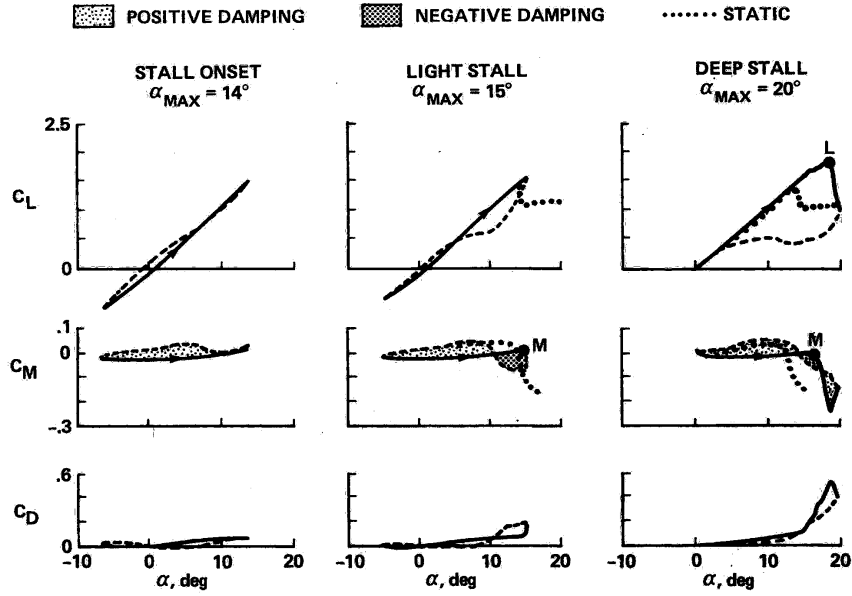
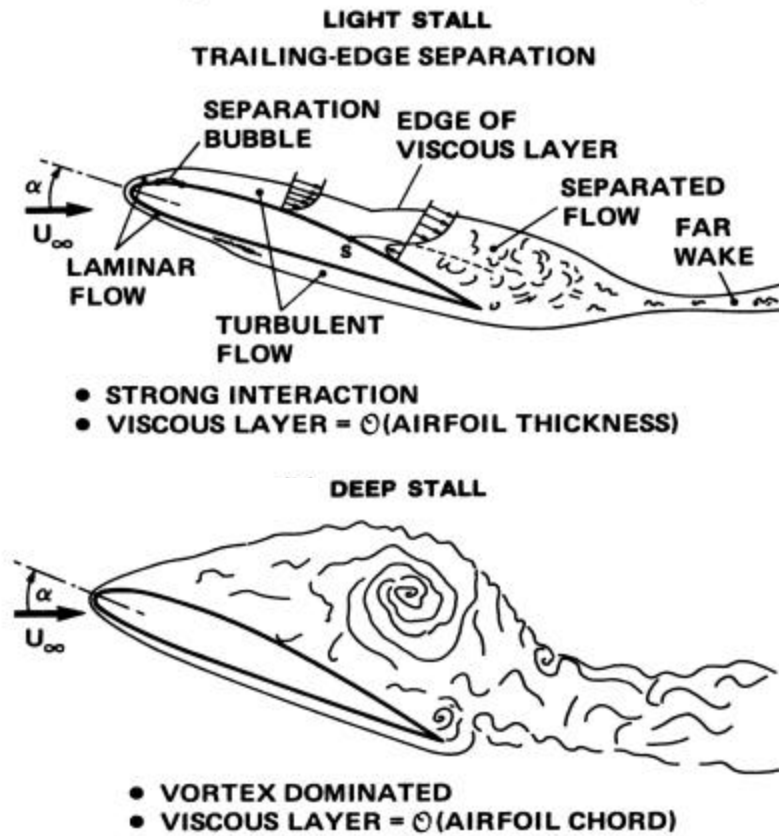


Figure 1.2: Illustration of flow near a Gurney flap as suggested by Liebeck. (From Liebeck, Ref. 1)



(a)



(b)

Figure 1.3: (a) Unsteady forces and moments in the three dynamic-stall regimes:  $M_{\dot{\gamma}}=0.3$ ,  $k=0.10$ ,  $a=a_0+10^\circ\sin(\omega t)$ . (b) Sketches of flow fields during light and deep dynamic stall. (From McCroskey, Ref. 13)

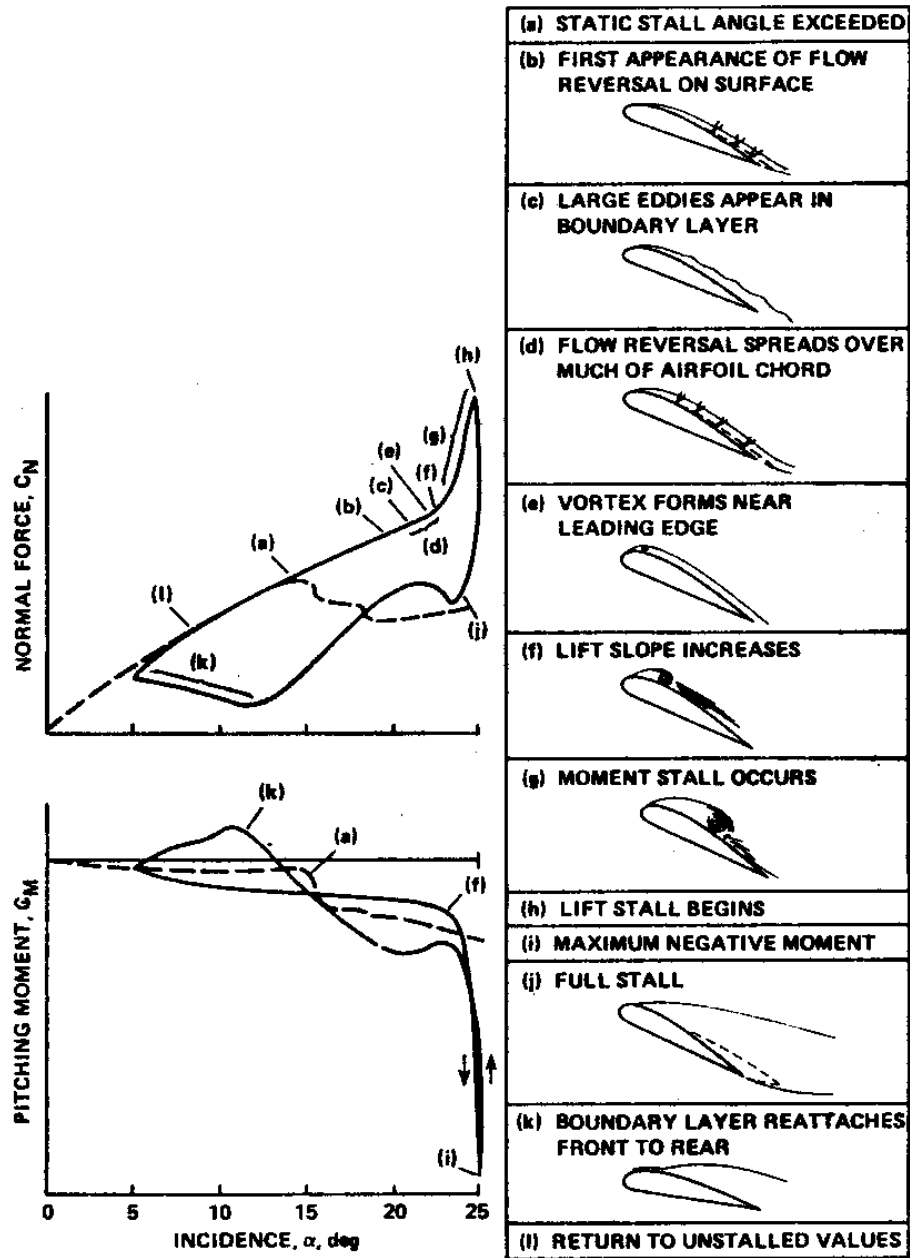
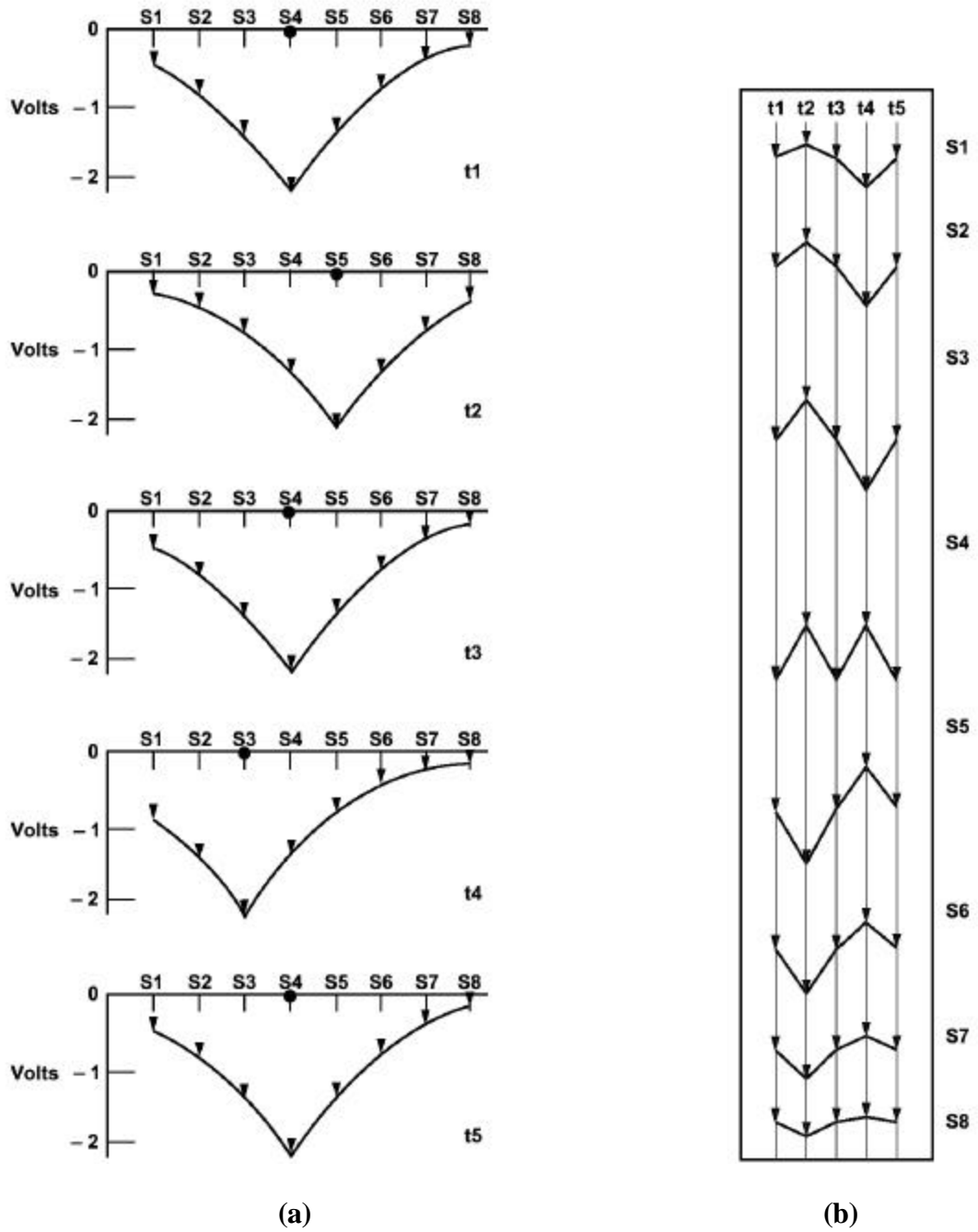
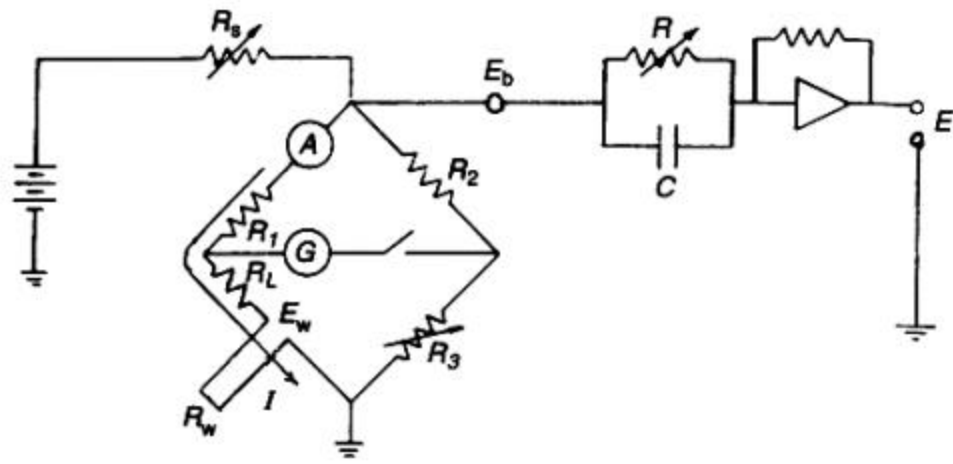


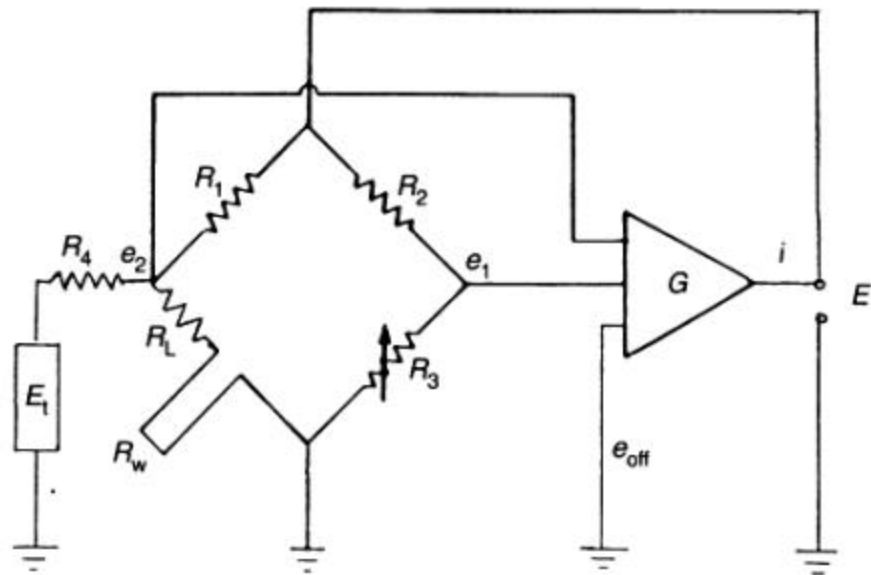
Figure 1.4: Sequence of events leading up to dynamic stall. (From Carr, Ref. 14)



**Figure 1.5: Phase reversal illustration. (a) Output voltage as a function of sensor location at five instants in time. (b) Output voltage as a function of time at eight sensor locations. (From Moes et al, Ref. 44)**



(a)



(b)

Figure 1.6: Circuit diagram of (a) constant current anemometer and (b) constant temperature anemometer. (From Comte-Bellot, Ref. 45)

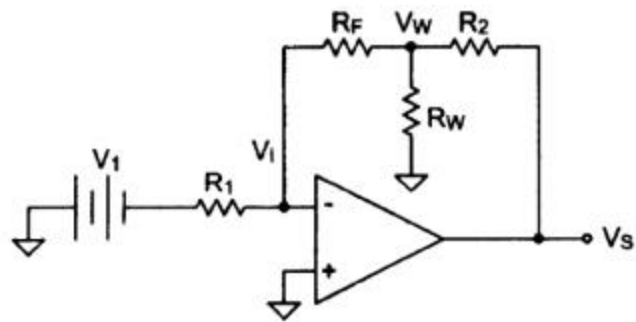
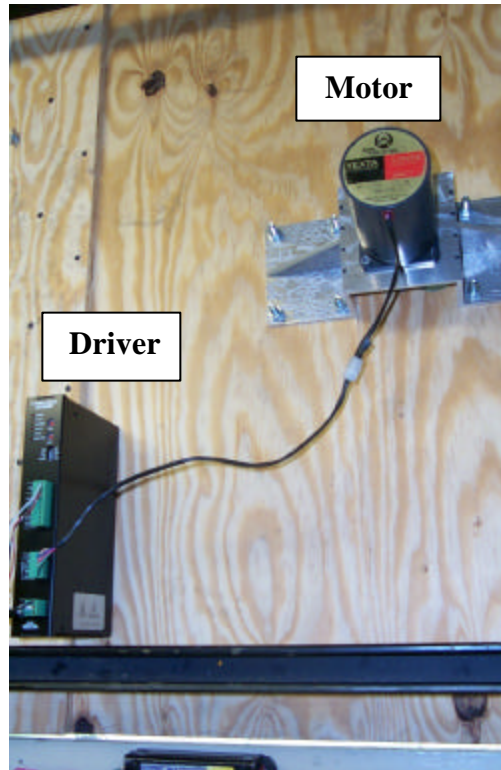


Figure 1.7: Circuit diagram of a constant voltage anemometer. (From Sarma, Ref. 47)



**Figure 2.1:** *NACA0012* airfoil model mounted in the wind tunnel.



**Figure 2.2: Stepper motor/driver package located on the top of the wind tunnel test section.**

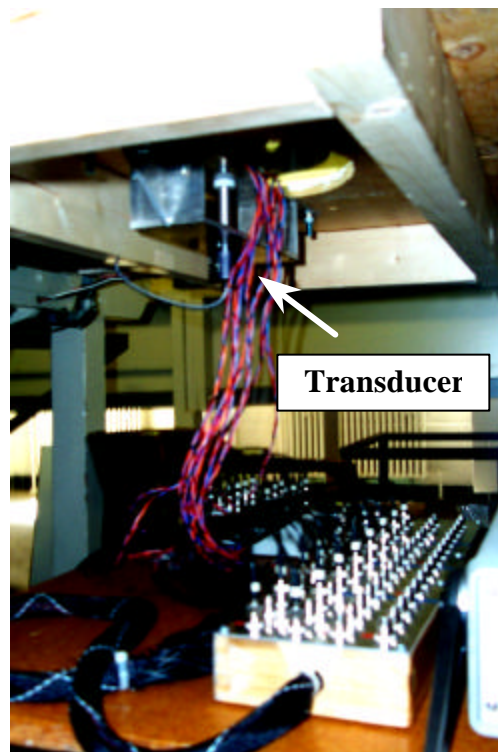


**Figure 2.3: Rotary variable inductance transducer mounted under the wind tunnel test section.**

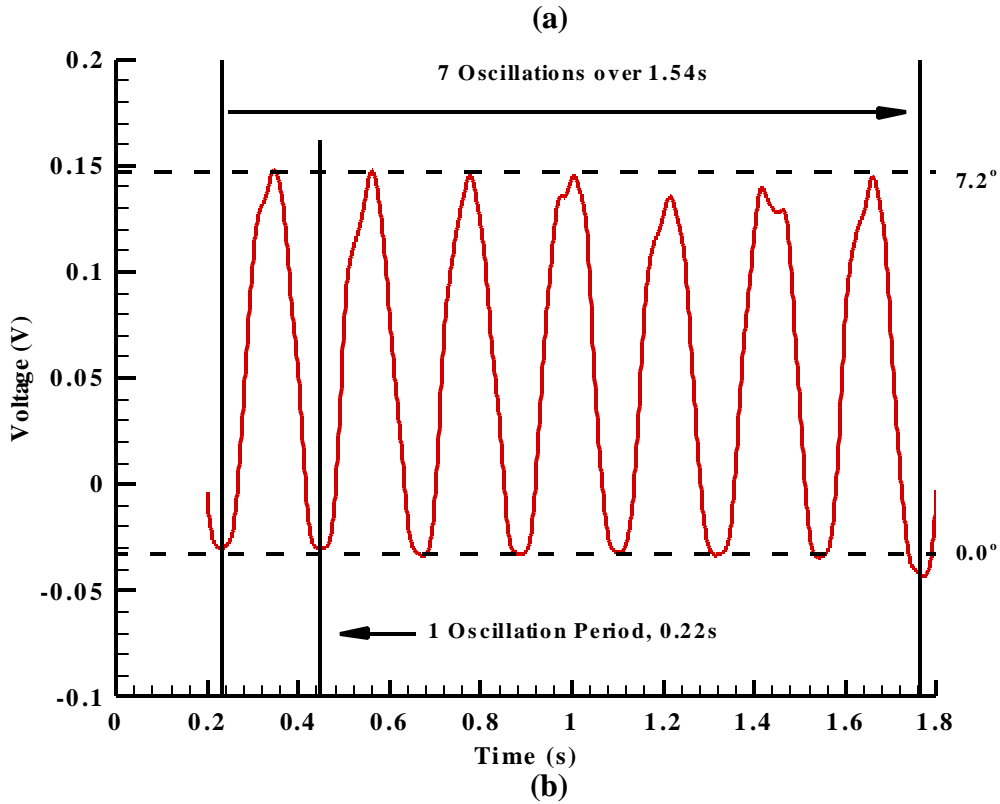
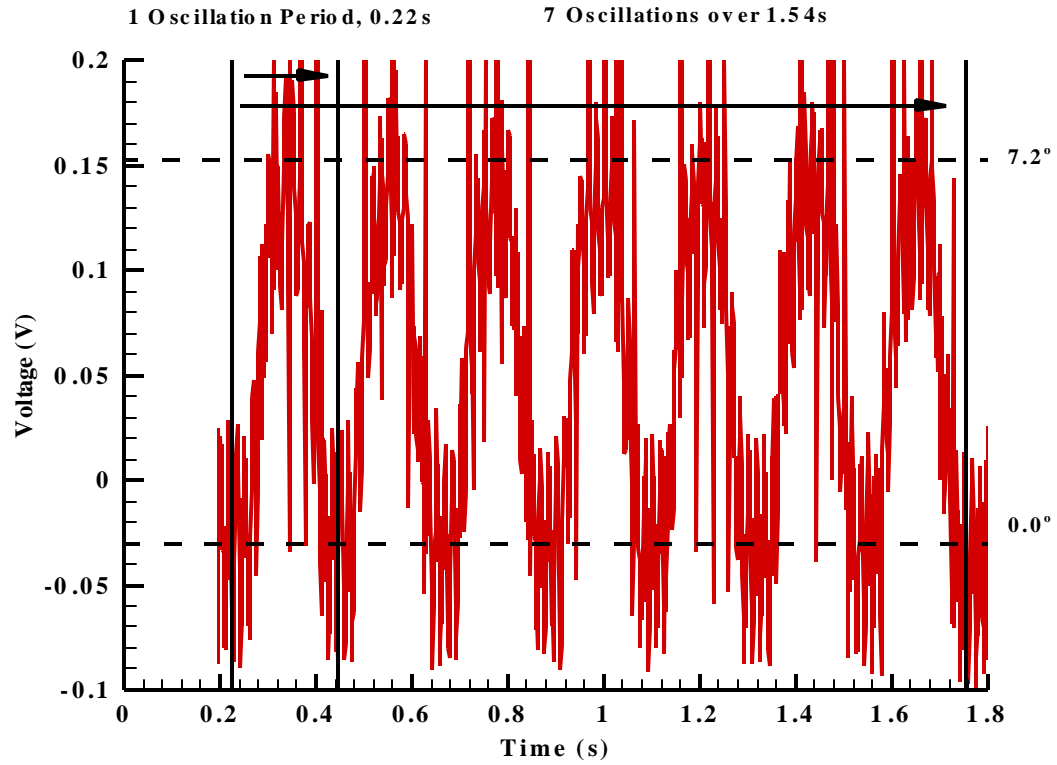
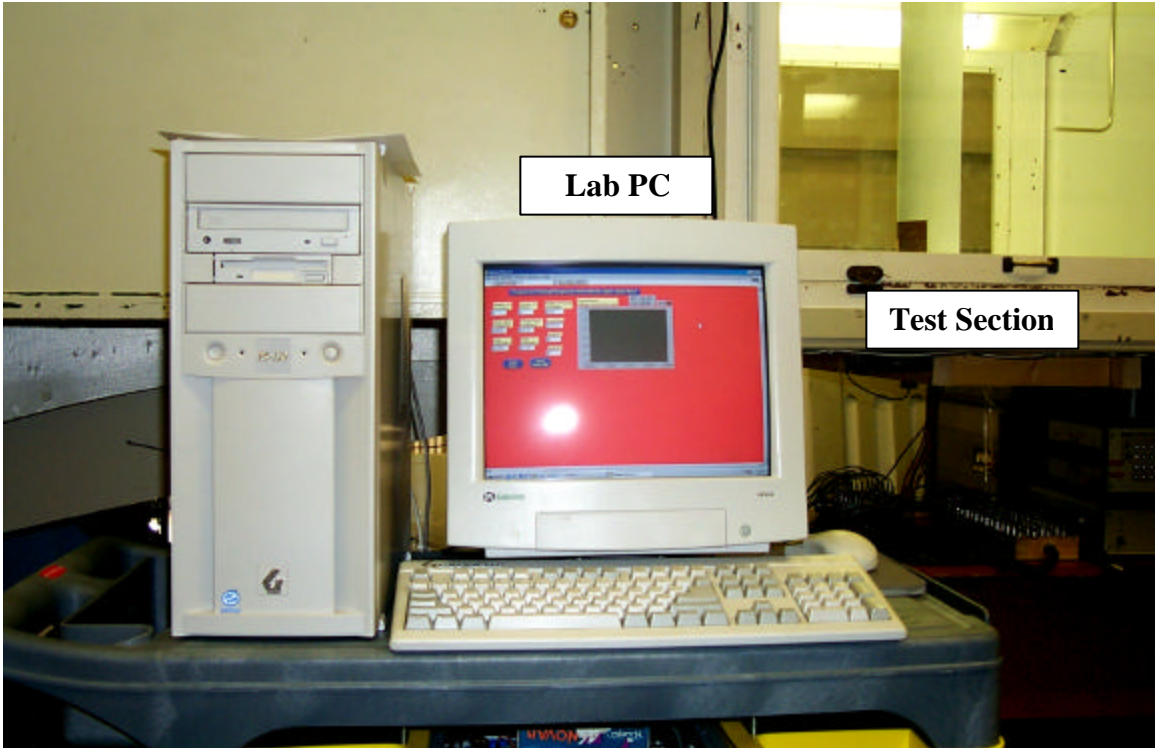


Figure 2.4: Output from inductance transducer for airfoil with a 2.5% chord Gurney flap oscillated for 10 periods to  $\alpha_{\max}=7.2^\circ$  at  $Re=192,000$ . (a) unfiltered data and (b) filtered data.



**Figure 2.5: Laboratory PC. The LabVIEW interface that is used to control the motor and obtain transducer data is shown on the monitor.**



**Figure 2.6: Connection pins for the data acquisition board.**

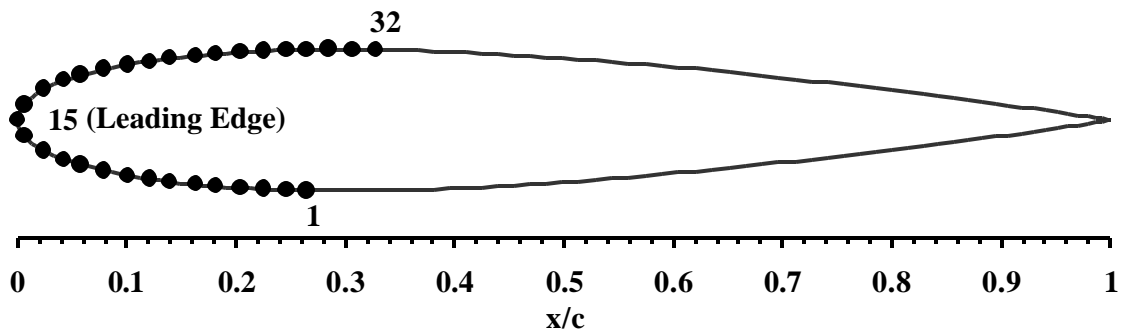


Figure 2.7: Cross-sectional view of the *NACA0012* airfoil showing hot-film sensor locations.

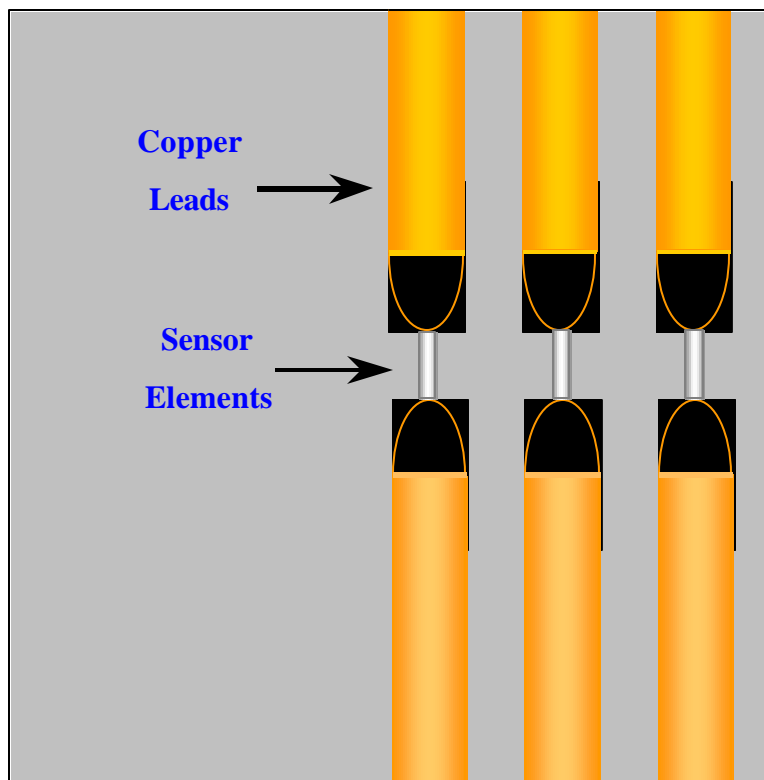
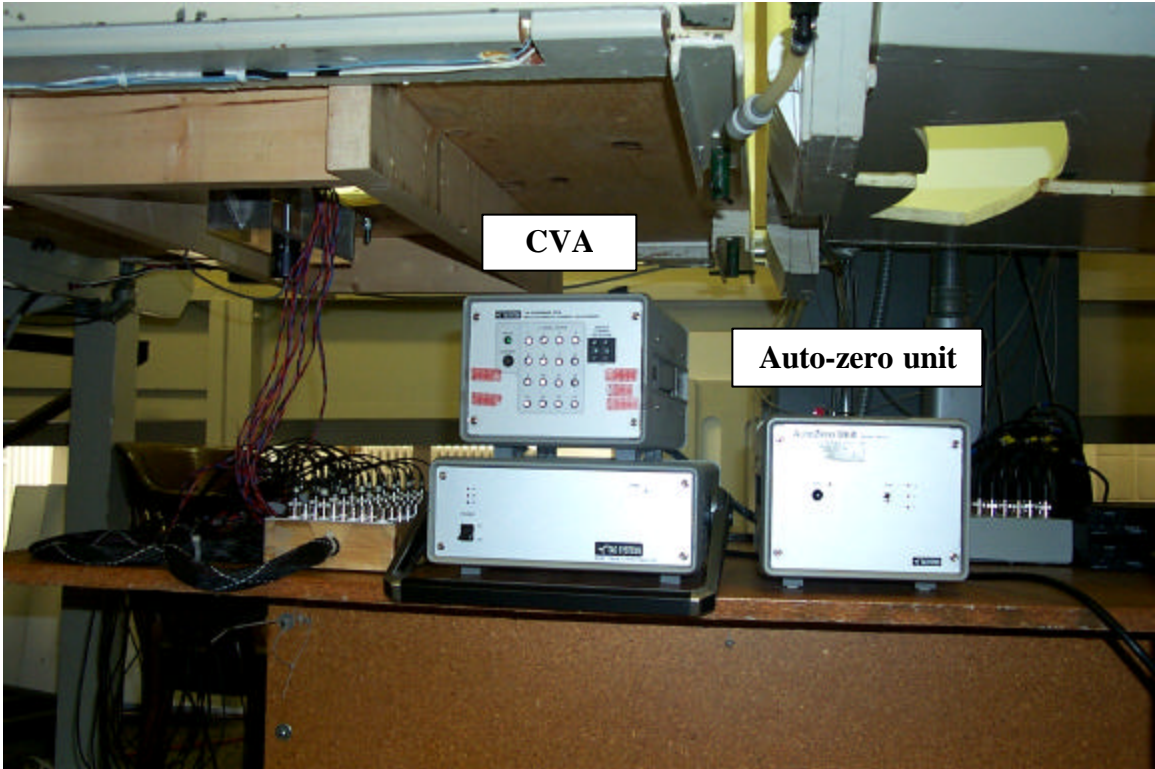
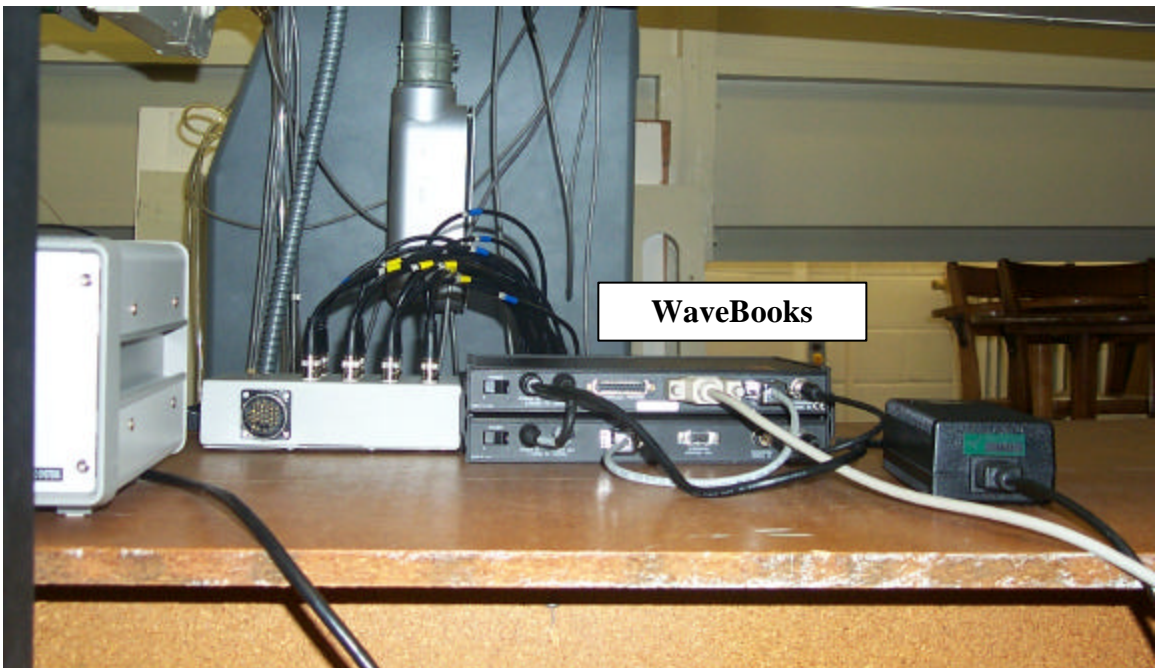


Figure 2.8: Close-up drawing of hot-film elements and copper leads.



**Figure 2.9: 16-channel constant voltage anemometer system and auto-zero unit.**



**Figure 2.10: IOtech<sup>®</sup> digitizers located beneath wind tunnel.**

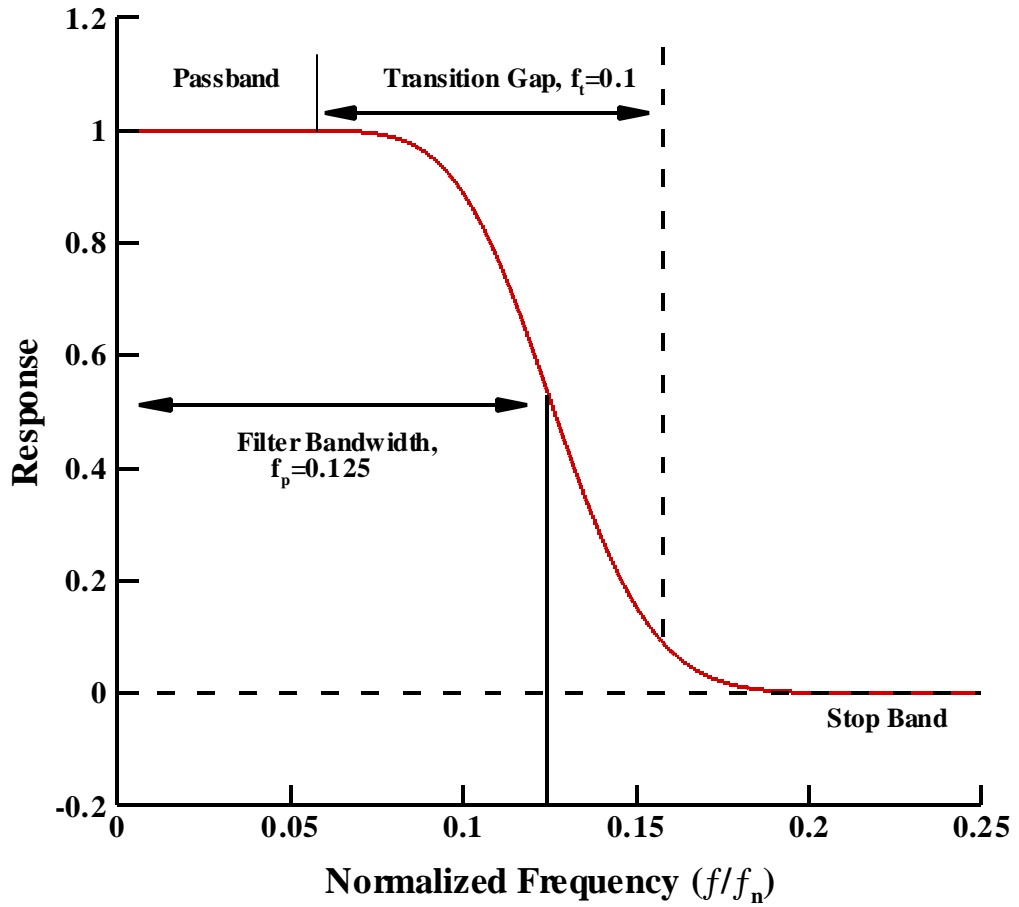
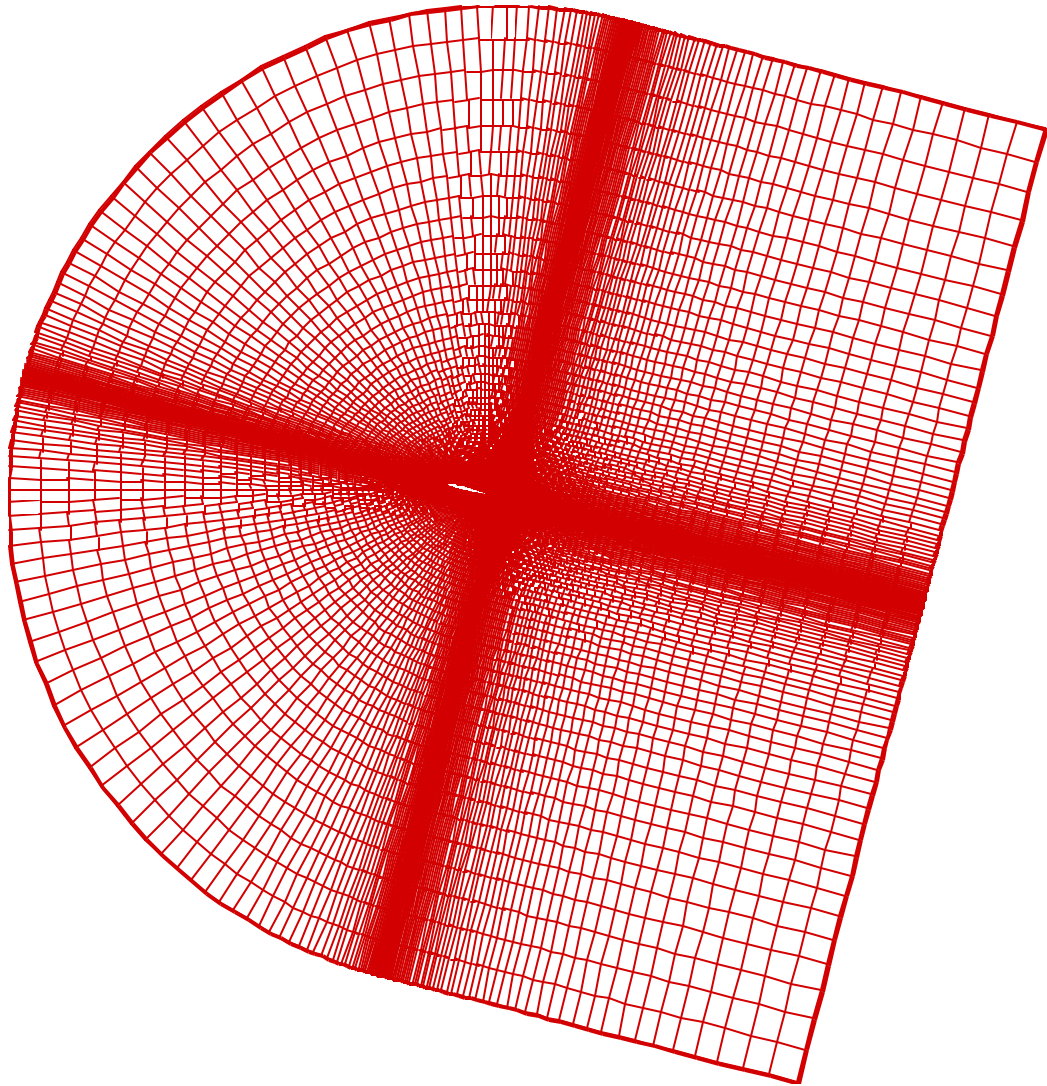


Figure 2.11: Frequency response of the digital low-pass filter.



**Figure 2.12: Computational grid at  $\alpha=14.4^\circ$ . Grid dimensions 438  $\times$  100.**

**Click [HERE](#) for 2<sup>nd</sup> Half of the Thesis:**

**Chapter 3 Figures and Chapter 8 Appendices**